RESEARCH ARTICLE

Key Points:
- We present tomographic images of the crust and upper mantle of the Mid-Atlantic Ridge (Rainbow area) made from *P* wave refraction data
- Along ridge segments, the crust is cold, brittle, and ~4-5 km thick and probably forms by repeated injection of small melt bodies
- Rainbow massif is capped by cool, altered mantle rocks; the interior is hot and relatively unaltered and deforms in the brittle regime

Correspondence to:
R. A. Dunn,
dunnr@hawaii.edu

Three-Dimensional Seismic Structure of the Mid-Atlantic Ridge: An Investigation of Tectonic, Magmatic, and Hydrothermal Processes in the Rainbow Area

Robert A. Dunn[1] [iD], **Ryuta Arai[1,2]** [iD], **Deborah E. Eason[1]** [iD], **J. Pablo Canales[3]** [iD], **and Robert A. Sohn[3]** [iD]

[1]Department of Geology and Geophysics, School of Ocean and Earth Science and Technology, University of Hawai'i at Mānoa, Honolulu, HI, USA, [2]Research and Development Center for Earthquake and Tsunami, Japan Agency for Marine-Earth Science and Technology, Yokohama, Japan, [3]Department of Geology and Geophysics, Woods Hole Oceanographic Institution, Woods Hole, MA, USA

Abstract To test models of tectonic, magmatic, and hydrothermal processes along slow-spreading mid-ocean ridges, we analyzed seismic refraction data from the Mid-Atlantic Ridge INtegrated Experiments at Rainbow (MARINER) seismic and geophysical mapping experiment. Centered at the Rainbow area of the Mid-Atlantic Ridge (36°14'N), this study examines a section of ridge with volcanically active segments and a relatively amagmatic ridge offset that hosts the ultramafic Rainbow massif and its high-temperature hydrothermal vent field. Tomographic images of the crust and upper mantle show segment-scale variations in crustal structure, thickness, and the crust-mantle transition, which forms a vertical gradient rather than a sharp boundary. There is little definitive evidence for large regions of sustained high temperatures and melt in the lower crust or upper mantle along the ridge axes, suggesting that melts rising from the mantle intrude as small intermittent magma bodies at crustal and subcrustal levels. The images reveal large rotated crustal blocks, which extend to mantle depths in some places, corresponding to off-axis normal fault locations. Low velocities cap the Rainbow massif, suggesting an extensive near-surface alteration zone due to low-temperature fluid-rock reactions. Within the interior of the massif, seismic images suggest a mixture of peridotite and gabbroic intrusions, with little serpentinization. Here diffuse microearthquake activity indicates a brittle deformation regime supporting a broad network of cracks. Beneath the Rainbow hydrothermal vent field, fluid circulation is largely driven by the heat of small cooling melt bodies intruded into the base of the massif and channeled by the crack network and shallow faults.

1. Introduction

Seafloor spreading along mid-ocean ridges is accommodated via a combination of tectonic extension and magmatic intrusion. Along slow spreading ridges (<60 mm/yr full spreading rate), where heat input from below is low relative to cooling rate, the lithosphere tends to be thicker and faulting accommodates a larger proportion of the extension as compared to faster spreading ridges (e.g., Parson et al., 2000; Toomey et al., 1985; Tucholke & Lin, 1994). Melt supply also tends to be lower and less uniform, and seismic studies suggest that heat supply is insufficient to stabilize long-lived, semicontinuous axial melt lenses, as observed in the shallow crust beneath faster spreading ridges (e.g., Detrick et al., 1987). Petrologic studies indicate that lower melt supply correlates with deeper magma storage (e.g., Eason & Sinton, 2006; Grove et al., 1992; Herzberg, 2004) and lesser degrees of magma mixing and chemical homogenization (cf. Rubin & Sinton, 2007, and references therein).

At a given spreading rate, differences in magma intrusion and storage are thought to play an important role in modulating extensional faulting by modifying lithospheric temperature, thickness, and tensile stress at the ridge axis (e.g., Searle & Escartín, 2004). This is supported by a strong correlation between melt supply and faulting style observed along individual slow spreading ridge segments (e.g., Shaw, 1992). Near segment centers, bathymetric highs, gravity lows, and seismic refraction data indicate thicker crust—and by inference higher melt supply—on average; conversely, the thinnest crust is often found near segment ends where melt supply is inferred to be relatively low (e.g., Canales, Detrick et al., 2000; Hooft et al., 2000; Kuo & Forsyth, 1988; Sinha & Louden, 1983). Areas of the ridge with relatively high melt supply form closely spaced faults with

smaller throws, while areas with low melt supply form large, long-lived detachment faults that accumulate offsets of a kilometer or more (e.g., Shaw, 1992; Shaw & Lin, 1993). In some areas with prolonged magma starvation, lower crustal and ultramafic rocks can be exposed directly at the seafloor, exhumed by long-lived detachment faulting and oceanic core complex (OCC) formation (Cann et al., 1997; MacLeod et al., 2009; Sauter et al., 2013; Tucholke et al., 1998).

Despite its relatively low-average magma supply and inferred deeper melt storage, the slow-spreading Mid-Atlantic Ridge (MAR) hosts robust hydrothermal systems with some of the highest heat outputs currently known (e.g., the Rainbow, Lucky Strike, and TAG hydrothermal fields). The prevalence of hydrothermal vent fields in settings dominated by tectonic extension, such as core complexes (e.g., Douville et al., 2002), suggests that on a local scale hydrothermal output is likely governed by additional factors, such as the depth and efficiency of fluid circulation, and temporal variations in melt supply and melt storage depth. At a given spreading rate, observations point to a general model wherein local variations in melt supply play a fundamental role in modulating the relationship between tectonic opening, crustal formation, and axial thermal structure (e.g., Behn & Ito, 2008; Buck et al., 2005; Cannat et al., 2006; Olive et al., 2010; Tucholke et al., 2008). However, a weakness of such models is the paucity of information on the subsurface structure of these systems. The dynamics of core complex formation and evolution, the origin of hydrothermal systems, and the extent to which hydrothermal cooling controls magma storage depth (or vice versa) and crustal construction continue to be matters of debate (e.g., Chen, 2004; Lowell et al., 2013; MacLeod et al., 2009; McCaig & Harris, 2012; Phipps Morgan & Chen, 1993).

To explore these interactions, a set of geophysical experiments collectively known as the MARINER (Mid-Atlantic Ridge INtegrated Experiments at Rainbow) study were conducted in the Rainbow region (35°45′–36°35′N) of the MAR. The experiments included sonar mapping, gravity and magnetics, and multiple seismic surveys. Results of the shipboard sonar and geopotential survey from this cruise were published in Paulatto et al. (2015) and Eason et al. (2016); results from a multichannel seismic (MCS) reflection survey, using a towed streamer system, were published in Canales et al. (2017); and results from a microseismicity study of the area are reported in Horning (2017). In this paper, we present three-dimensional seismic images produced by seismic refraction tomography.

2. Study Area

The study area is located along the MAR, 500 km southwest of the Azores triple junction (Figure 1a). Along this section of the MAR, the spreading axis consists of a series of mostly right-stepping ridge segments bounded by transform offsets and nontransform discontinuities (NTDs). The study area itself contains four echelon right-stepping ridge segments separated by three NTDs (Figure 1b) that translate the ridge axis by almost 30 km in total. The central NTD is the largest and accommodates about 15 km of the total offset. Hereafter referred to as the Rainbow NTD, it hosts the Rainbow massif, a 15 km wide domed topographic high. The full spreading rate for the area is ~22 mm/yr in a WNW-ESE direction (Argus et al., 2011) oriented 80–85° relative to the trends of individual ridge segments (Figure 1b).

From south to north, the four ridge segments in the study area are S AMAR, AMAR Minor S, AMAR Minor N, and AMAR (Figure 1b) (after Paulatto et al., 2015 and predecessors (e.g., German et al., 1996). These ridge segments are characterized by wide axial rift valleys (up to ~8 km width), with water depths typically >2.5 km, bounded by steep fault scarps. Paulatto et al. (2015) estimated tectonic strain values of 20–30% for the S AMAR and AMAR segments, ~40% for AMAR Minor S and the AMAR Minor N, and 60–80% for the Rainbow NTD. The valley floor of three of the four segments is paved with lava, as indicated by high sea-floor backscatter (Eason et al., 2016; Parson et al., 2000) and basaltic rock samples (Gale et al., 2013; Sigurdsson, 1981; Stakes et al., 1984). The fourth segment, AMAR Minor N, is more heavily sedimented, with only a small patch of moderately high backscatter volcanic seafloor near its northern terminus.

Within each segment, fault throws and spacing vary such that faults tend to be steeper and more finely spaced with smaller offsets near segment centers (Paulatto et al., 2015), where bathymetric highs and gravity lows suggest greater crustal thickness and magma supply. As magma supply decreases and the axial valley deepens toward segment ends, extension is accommodated on fewer, more widely spaced faults with greater heave. This progression culminates in large OCC-forming detachment faults at the Rainbow NTD.
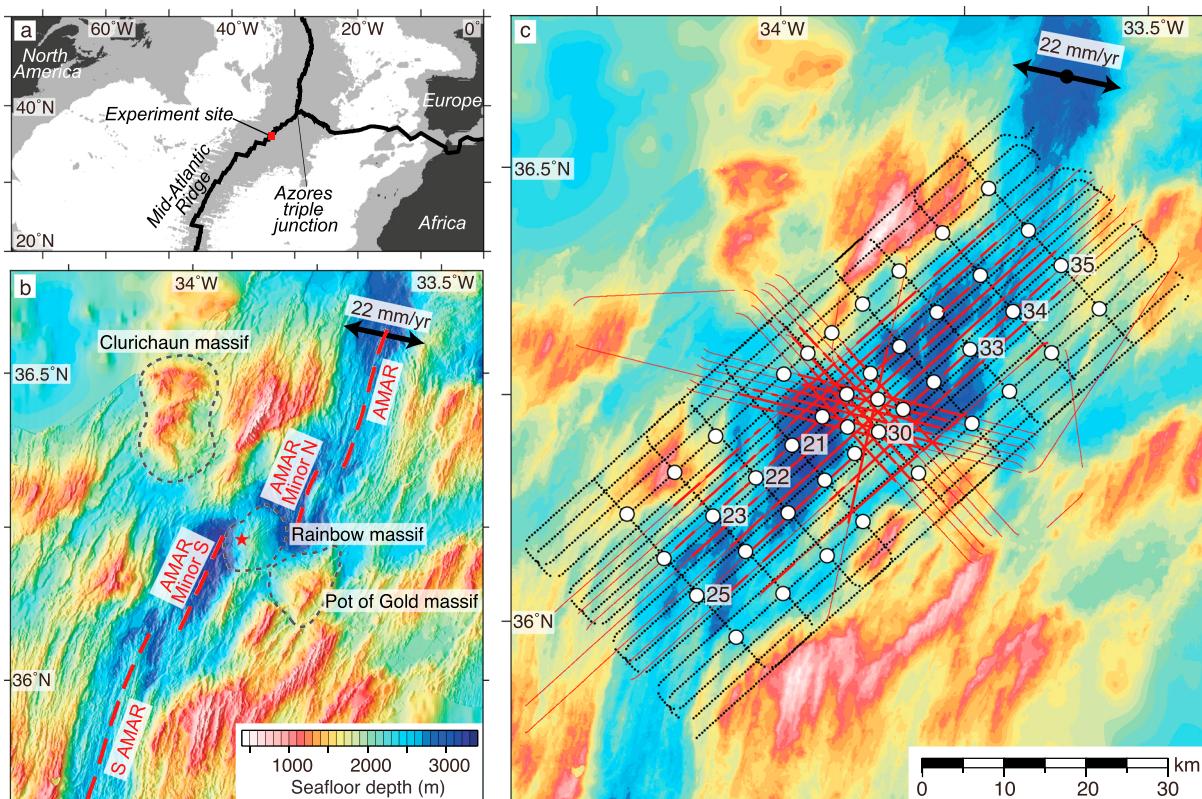
Figure 1. (a) Regional tectonic map of the Mid-Atlantic Ridge (MAR). Light gray areas delimit regions with a seafloor depth of <4,000 m, highlighting high-standing topography along the MAR. Black solid lines are plate boundaries by Bird (2003). Red box indicates location of Figures 1b and 1c. (b) Bathymetry map of the experiment area; seafloor depth (color scale) is shaded by slope. The experiment spans four ridge segments (red dashed lines). Rainbow and other massifs are labeled and outlined by gray dashed curves. A red star indicates the location of the Rainbow vent field. (c) Layout of the seismic experiment. Open circles indicate ocean bottom seismograph locations; numbered locations correspond with stations indicated in Figures 2 and 3. Black and red dotted lines indicate locations of air gun pulses used here from the wide-angle and multichannel seismic profiles (red thin lines), respectively.

Extending across the study area is the trace of the Rainbow NTD. This NTD has produced a broad "wake" of disrupted seafloor morphology characterized by deep seafloor, disrupted fault patterns, broad and heavily sedimented basins, and high-mantle Bouguer gravity values, indicating thin crust and a persistent low melt supply for at least 3 Myr (Paulatto et al., 2015). The wake of the NTD is lined by a string of domed features presumed to be OCCs, including the Rainbow, Pot of Gold, and Clurichaun massifs (Paulatto et al., 2015) (Figure 1b). While only the Rainbow massif has been sampled, the morphology and high gravity anomalies of each massif suggest uplifted lower-crustal/mantle material.

Samples from the surface of the Rainbow massif are dominated by peridotite (harzburgite and dunite) with variable degrees of serpentinization (Andreani et al., 2014; Ildefonse et al., 2008). Gabbroic rocks (troctolite, olivine gabbro, and gabbronorite) have been sampled at a few locations on the massif, and variably altered basalts have been recovered from the northeastern and southwestern slopes of the massif (Andreani et al., 2014). Abyssal sediments cover the western and easternmost portions of the massif, down to the rift valley floor (Andreani et al., 2014; Eason et al., 2016; Gaill et al., 2007; Ildefonse et al., 2008). Although many OCCs exhibit a corrugated surface associated with mature detachment faults (Cannat et al., 2006; Tucholke et al., 1998), such morphological features are unclear here. Instead, the massif is crosscut by two sets of secondary normal faults oriented north-south and southwest-northeast. The detachment fault itself is inferred to be inactive due to the widespread sediment cover, lack of recent detachment fault exposure, presence of the secondary faults, and absence of seismicity along any detachment fault plane (Andreani et al., 2014; Horning, 2017).

An active hydrothermal vent field, the Rainbow field, is located on the western flank of the massif (Figure 1b) at the intersection of the secondary fault structures (Andreani et al., 2014; German et al., 1996). The field

extends over a 200 × 100 m^2 area and is mainly composed of 10 black smoker chimneys, with vent fluid temperatures up to ~365°C and several other active and inactive vents (Charlou et al., 2002; Tivey & Dyment, 2010). It is estimated that the vent field has been active as a high-temperature feature for at least ~8,000 years (Cave et al., 2002) and perhaps up to ~23,000 years (Kuznetsov et al., 2006). Two additional inactive low-temperature fields are located 1–2 km NE and E of the Rainbow field (Lartaud et al., 2010, 2011). At least one study failed to find evidence for significant diffuse flow on the massif outside the vent fields (German et al., 2010). The Rainbow vent fluids have high concentrations of chloride, metals, hydrogen, and methane (Charlou et al., 2002; Douville et al., 2002). The high chloride content is consistent with brine formation by phase separation, while high hydrogen is indicative of serpentinization reactions resulting from seawater interaction with the ultramafic rocks of the massif (Charlou et al., 2002). Although an estimated ~40% of the heat is generated from cooling of the hot uplifted mantle and to a lesser extent by exothermic serpentinization reactions (Allen & Seyfried, 2004; Canales et al., 2017), some aspects of the fluid chemistry are consistent with interaction with gabbroic bodies (Charlou et al., 2002), and the vent field's high heat flux (~0.5 GW) and fluid volume flux (~450 L/s) require a magmatic heat source (Charlou et al., 2002; German et al., 2010). The seismic reflection study of the MARINER experiment (Canales et al., 2017) revealed a series of subhorizontal reflectors within the massif and below the vent field interpreted as sill-like intrusions, some of which may be hot or partially molten and supply heat for the Rainbow hydrothermal field as they crystallize and cool.

3. Seismic Data

The seismic data were collected using the R/V *Marcus G. Langseth* (cruise MGL1305) and its 36-element 6,600 cubic inch airgun array. The seismic experiment, centered on the Rainbow massif, extends 80 km in the ridge-parallel direction and 32 km across the ridge (Figure 1c). For 3-D refraction tomography, 46 ocean bottom seismometers (OBSs) were deployed within this rectangular area (43 provided full data sets) with an average spacing of 7 km but with increasing density toward the Rainbow massif. Each OBS contained a hydrophone and 1- or 3-component geophone and recorded at a sampling rate of 200 Hz. After recovery, OBS seafloor positions were determined using the traveltimes of the direct water wave for shots within 5 km of an instrument and a Bayesian grid search algorithm (Dunn & Hernandez, 2009). The 1σ location uncertainties are <10 m. Approximately 3,800 airgun pulses were triggered every ~450 m along 26 refraction lines (black lines in Figure 1c; ~1,700 km of profiles). During the experiment, 21 lines of MCS reflection profiles were also carried out with a nominal source spacing of 37.5 m (thin red lines in Figure 1c). At the time of the MCS experiment, the inner 20 OBSs of the array were on the seafloor and the arrival traveltimes from those sources were also included in the tomographic analysis (red thick lines in Figure 1c).

The seismic data were processed via a sequence of steps prior to traveltime picking. Because different sensor types were used, the instrument responses were first removed from the data, then the data were band-pass filtered with a minimum phase 5–20 Hz filter, and the amplitudes scaled for geometric spreading loss. In a few cases, the hydrophone and vertical component data were stacked to increase the signal-to-noise ratio. The traces were adjusted via static time corrections for seafloor topography to better align the waveforms for easier traveltime identification. The first arrivals of compressional waves were manually picked using the best-quality channel (either the vertical geophone or hydrophone channel). Including all estimated experimental errors (for instrument position, time base, shot position, picking uncertainties, etc.), the root-mean-square uncertainty of the traveltimes was 32 ms.

For sources ~2 to 10 km from an instrument, the first energy to arrive is a refraction from seismic layer 2 (*P2*) with apparent velocities of ~3.0–5.0 km/s (Figure 2). Thereafter, layer 3 refractions (*P3*) with apparent velocities typical of lower oceanic crust (6.0–7.2 km/s) occur out to ~15 km distance, but these phases are seldom observed in the central part of the experiment near the Rainbow massif (Figures 2 and 3). At farther distances, first arrivals are refractions with apparent velocities of ≥7.5 km/s, typical of the mantle (*Pn*), which are identified out to >40 km. There is usually a change in slope of the arrivals, from crustal to mantle velocities, that sometimes corresponds with higher amplitudes. However, despite high-quality data, there is little evidence for reflected arrivals from a Moho discontinuity (*PmP*) (Figure 2), indicating a relatively gradual crust-to-mantle transition on the scale of the seismic wavelength. Approximately 153,000 traveltime data (*P2*, *P3*, and *Pn* phases) were used in the tomographic analysis.
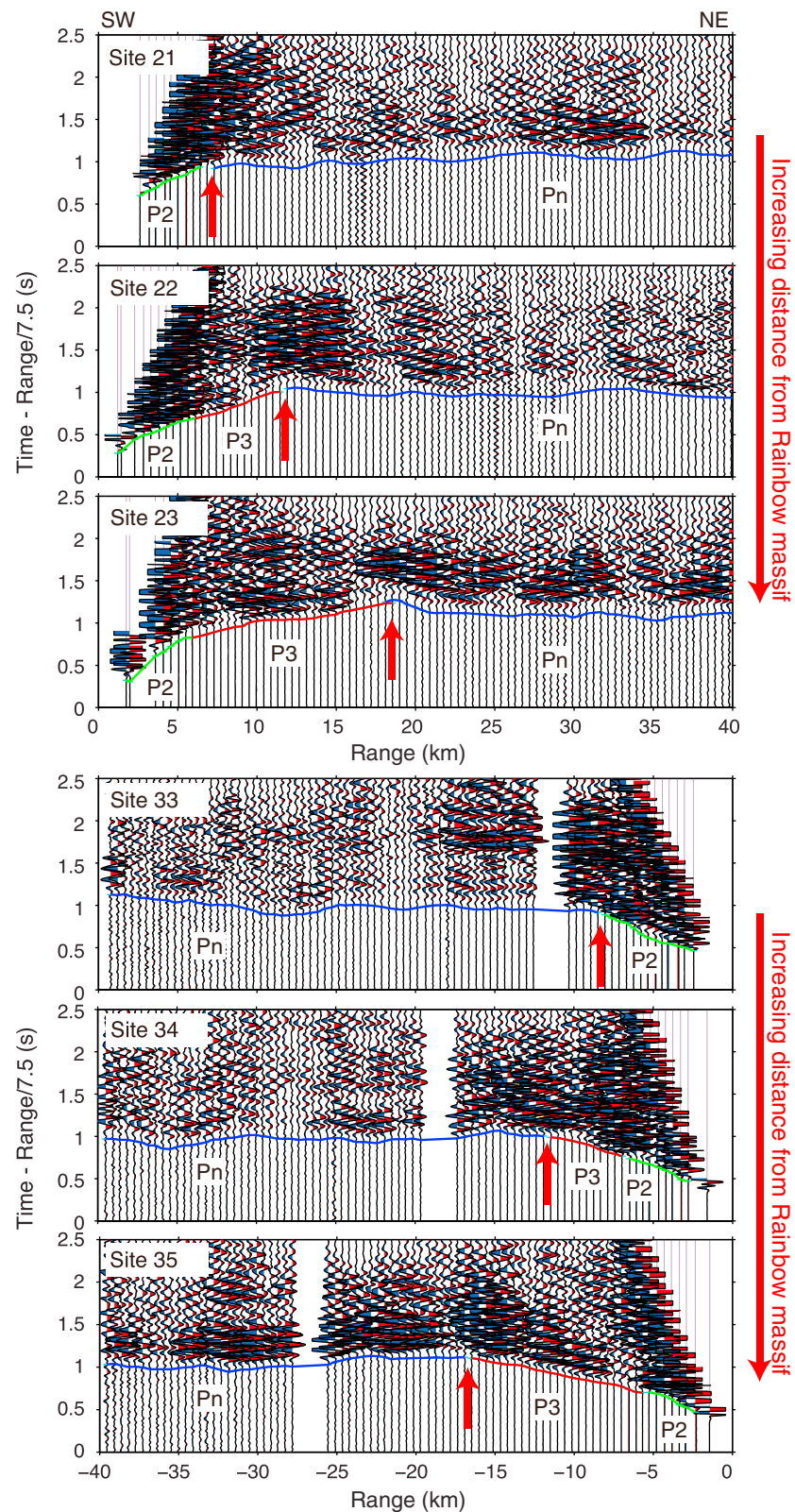
Figure 2. Examples of common-receiver-gather seismic record sections (corrected for seafloor topography). Solid lines of green, red, and blue indicate picked times of the seismic phases P2 (arrivals from the shallow low-velocity layer: either the upper crust or upper altered mantle where the crust is absent), P3 (lower crust), and Pn (mantle) phases, respectively. Phase identification is based on the slope of the arrivals and to some extent trace amplitudes. Red arrows indicate the (P2, P3)-Pn crossover distance.
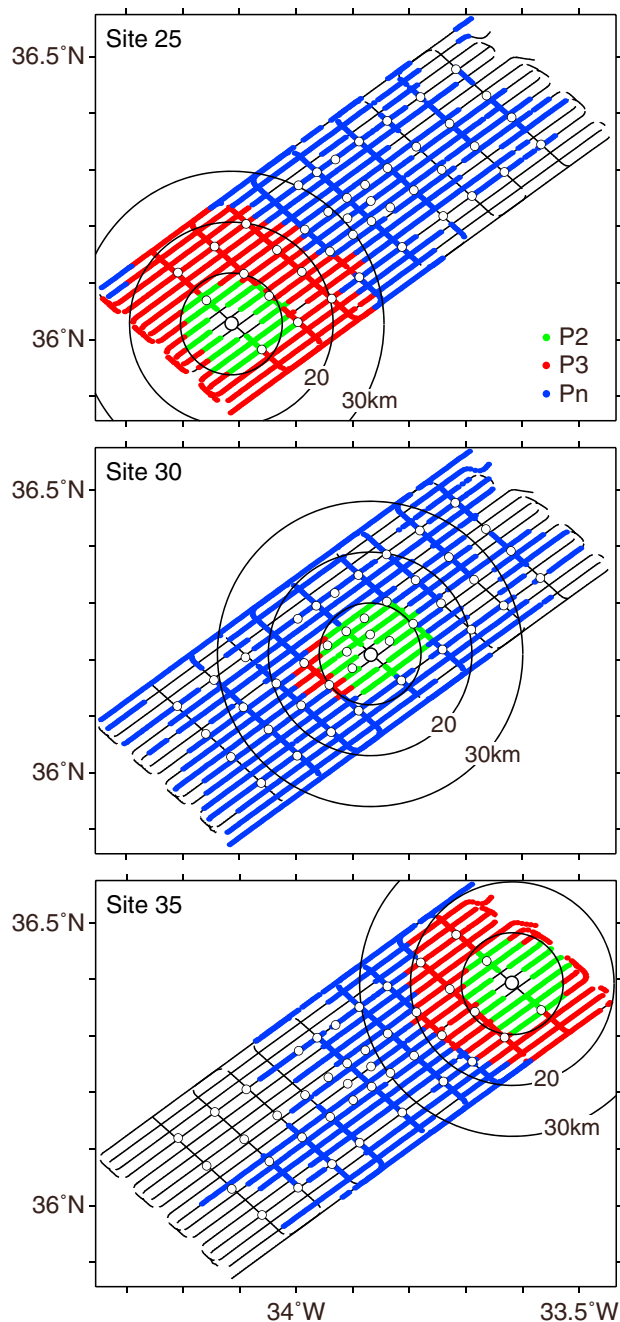
Figure 3. Pick types of first arrivals for each shot-receiver pair. White dots indicate OBS positions. Green, red, and blue dots correspond to P2, P3, and Pn phases, respectively. As in Figure 2, this plot shows larger P3-Pn crossover distances away from the Rainbow massif (sites 25 and 35) as compared to nearer (site 30). Around Rainbow, there are almost no P3 arrivals. Black circles about each station show radial distances of 10, 20, and 30 km.

In oceanic settings, Pn arrivals often have weak amplitudes compared to P3 arrivals and this is attributed to a low or even negative vertical velocity gradient in the upper mantle (e.g., McClain & Lewis, 1982; Minshull & White, 1996), possibly due to a high geothermal gradient. Here the Pn arrivals have relatively strong amplitudes compared to P3 arrivals, and there are distinct Pn arrivals extending across the length of the experiment. This indicates that there is a significant positive vertical velocity gradient, possibly due to a relatively low geothermal gradient and/or increasing proportion of ultramafic to mafic material with depth. The P3-Pn crossover distance (the distance between shot and receiver where Pn becomes a first arrival) is an approximate indicator of crustal thickness, with larger crossover distances indicating thicker crust. Crust farther from the Rainbow NTD appears to be thicker, with P3-Pn crossover points at >15 km range (e.g., sites 23 and 35 in Figure 2, and sites 25 and 35 in Figure 3). In contrast, crust nearer the Rainbow NTD is thinner, with P3-Pn (or P2-Pn) crossover points at 5–10 km (sites 21 and 23, Figure 2 and site 30 in Figure 3). At Rainbow, despite observations that mantle rocks outcrop across the massif, P2 arrivals are clearly present (site 30 in Figure 3), indicating a significant velocity reduction of the upper part of the massif relative to more typical mantle values, presumably due to porosity and advanced serpentinization, as observed in surface samples (Andreani et al., 2014).

4. Methods

Seismic imaging was carried out using an iterative tomographic technique that uses traveltime data to compute 3-D velocity structure (Dunn et al., 2005; Dunn & Martinez, 2011). For ray tracing, the forward problem included a finely spaced 3-D grid (250 m spacing laterally; 150 m vertically) of P wave velocity values, whose surface conforms to seafloor topography, overlain by a water layer. For the inverse problem, model parameters for isotropic slowness were spaced 0.5 km apart laterally. Vertically, the parameter spacing increased from 0.25 km at the surface to 1 km at the bottom of the volume (10.2 km below seafloor). Model parameters for azimuthal anisotropy were also included in this analysis (1.1 × 2.0 km laterally; increasing from 0.45 to 2.0 km vertically). The full anisotropy results will be presented in a separate publication, only the 1-D (depth-varying) solution is presented here. The inversion was regularized with adjustable smoothness and variance constraints to control solution stability and prevent statistical overfitting in the presence of noise. A grid search was performed by varying the strength of the horizontal and vertical smoothness constraints to determine an acceptable range of 3-D solutions that fit the data. The final velocity model was chosen by examining overall data fit and the results of checkerboard and spike resolution tests (see Appendix A and supporting information).

To obtain a stable starting model, first, a 1-D depth-varying velocity model was taken from a neighboring study area (Dunn et al., 2005). That model was then used to solve for a 3-D solution, which was then laterally averaged to create a new 1-D starting model. Several iterations were performed until the change in the 1-D model was not significant. The final 1-D model (red curve in Figure 4a) is generally typical for slow-spreading rate crust, with a ~1 km thick low-velocity layer at the top (seismic layer 2) characterized by a rapid increase from 2.5 km/s to 5.5 km/s. Underlying the low-velocity layer is a more gradual gradient that extends to depths of 4 km or
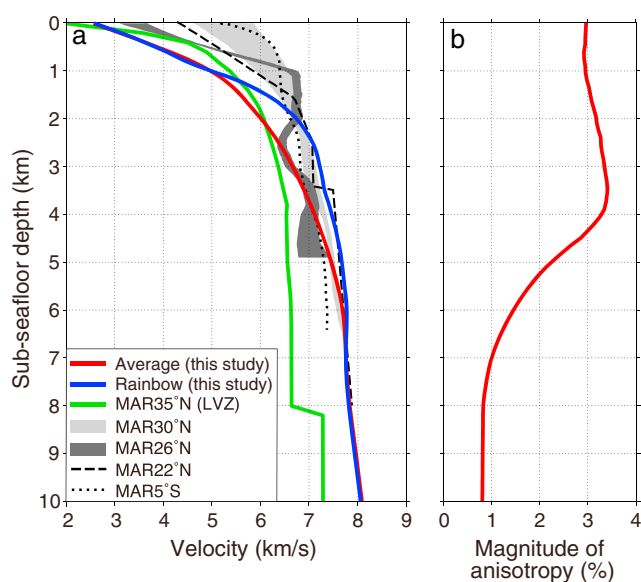
Figure 4. *P* wave velocity profiles. (a, b) Red curves are the isotropic and aniso-tropic profiles, respectively, used as the starting model. Taken from the 3-D solution, the blue thick curve is the profile beneath Rainbow massif. For comparison are average profiles from 30°N (Blackman & Collins, 2010), 26°N (Canales et al., 2007), 22°N (Dannowski et al., 2010), and 5°S (Planert et al., 2010); each area hosts oceanic core complexes. The profile for 35°N (green curve; Dunn et al., 2005) is taken from an area where there is a pronounced low-velocity feature extending from ~3 km depth into the mantle. In Figure 4b, the magnitude of anisotropy is defined as follows: $100 \, (V_{p\max} - V_{p\min})/V_{P,\text{average}}$.

more. There is a transition from lower-crustal values of ~6–7 km/s to mantle velocities of ≥7.5 km/s over a depth range of 3.5 to 5 km. As indicated by the seismic records (Figure 2) and the sparse evidence for Moho reflections, the crust–mantle transition occurs gradually in the vertical direction throughout most of the study area. Since this gradual transition occurs at different depths across the study area, it is even less distinct in the 1-D average model. The 1-D solution for the magnitude of anisotropy (Figure 4b) has values of ~3% in the top 4 km of the litho-sphere and thereafter decreases with depth. The fast direction of aniso-tropy lies along an azimuth roughly normal to the direction of plate spreading, as is expected for anisotropy caused by ridge-parallel cracks formed by tensile stress (e.g., Stephen, 1981). Anisotropy due to lattice preferred orientation of mantle minerals is expected to produce a fast direction oriented in the spreading direction and thus does not appear to be a dominant factor within the context of this average.

5. Results

Vertical cross sections from the 3-D tomographic image (oriented approximately parallel to the spreading direction), Figure 5 (left column), reveal many vertical undulations in velocity structure. Tests indicate that these features are well resolved (see Appendix A and sup-porting information). The close correspondence between these undu-lations and large fault scarps observed in bathymetry maps (Paulatto et al., 2015) indicates that this structure arises from the offset and rota-tion of large crustal blocks via normal faulting. In velocity anomaly images, Figure 5 (right column) (showing velocity variations relative to the 1-D model), the high-velocity portions of the bands tend to correlate with the exposed footwalls of large-offset faults or fault groupings. This indicates that faults uplift high-velocity material within the footwall, juxtaposing it next to lower-velocity material. These undulations are not an artifact of the topography of the seafloor, since they trend downward at angles consistent with the dip of exposed fault surfaces rather than stack vertically beneath the topography.

Correspondingly, map view slices of the seismic image (Figure 6) reveal sequences of prominent high- and low-velocity bands that parallel fault structures and result from these slices crosscutting the vertical undula-tions seen in Figure 5. The banding is clearest in lithosphere formed at the AMAR Minor S and AMAR Minor N ridge segments, immediately south and north of the Rainbow NTD, where tectonic strain estimates are higher than along the other segments (Paulatto et al., 2015). Lateral velocity gradients between opposite polarity bands are high, and some show up as prominent linear features in V_P gradient maps (Figure 7). Figure 8 shows selected map view slices of the seismic images along with overlays of fault scarps (from Paulatto et al., 2015). Overall, the bands appear mostly at depths <4 km, fading away to broader velocity variations at greater depth where mantle velocity values occur. Along the imaged portions of the S AMAR and AMAR segments, fault exposures are often more finely spaced with smaller throws, and the velocity undulations/banding is not as evident or blends together into larger dipping features, such as the long blue anomalies on the western side of profile A and eastern side of profile G in Figure 5. At the scale of the fault spacing (<0.5–1 km), the seismic image lacks sufficient resolution to reveal small-scale patterns associated with closely spaced faults. Some previous studies of mid-ocean ridges have reported velocity variations corresponding with fault locations (e.g., Canales, Collins, et al., 2000; Canales et al., 2007), but this study reports the most extensive and well-resolved images of such features to date, and the 3-D nature of the experiment enables the mapping of fault-related velocity variations along complete spreading segments for the first time.

On a broader scale, tomographic images also indicate segment-scale variations in crustal thickness and, by association, melt supply, with higher velocities and by inference thinner crust occurring at segment offsets. The principle observation is a wide band of higher-than-average velocities extending along the deep
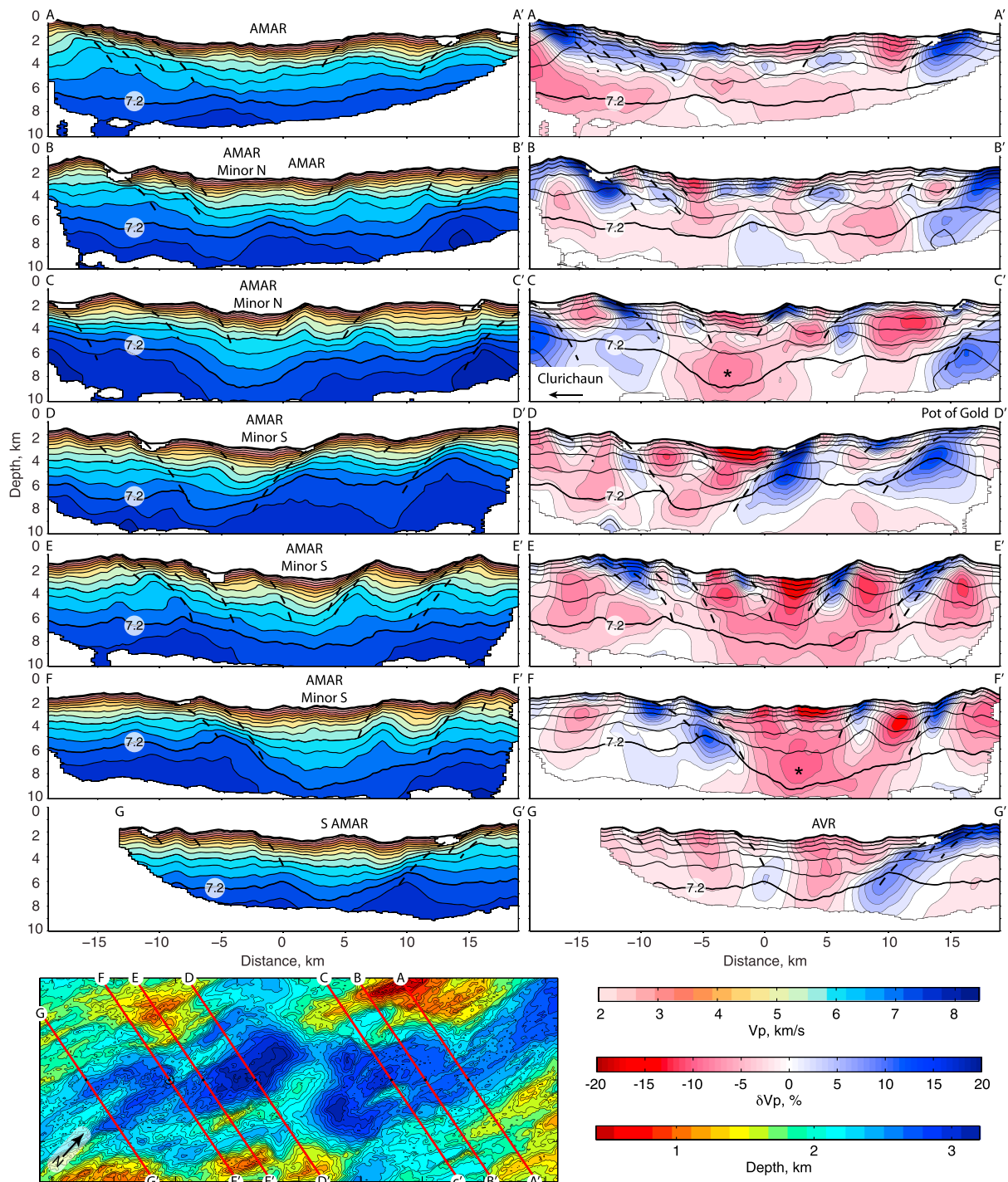
Figure 5. (left column) Vertical tomographic slices oriented approximately parallel to the spreading direction of V_P and (right column) V_P perturbation relative to the 1-D average profile of Figure 4a. The contour interval is 0.4 km/s for V_P plots and 2% change in V_P for perturbation plots. Overlain on the perturbation images are contours of V_P at 0.8 km/s spacing for reference. The 7.2 km/s contour (bold line) is labeled for reference. The locations of each panel are indicated by red labeled lines on the map (bottom). Dashed lines indicate fault location interpretations. Deep low-velocity regions beneath the ridge axes, such as in profiles C and F (indicated with a black asterisk), may reflect higher temperatures (see section 6). A mask (white areas) was applied to the images here and in subsequent figures to remove areas with low resolution.
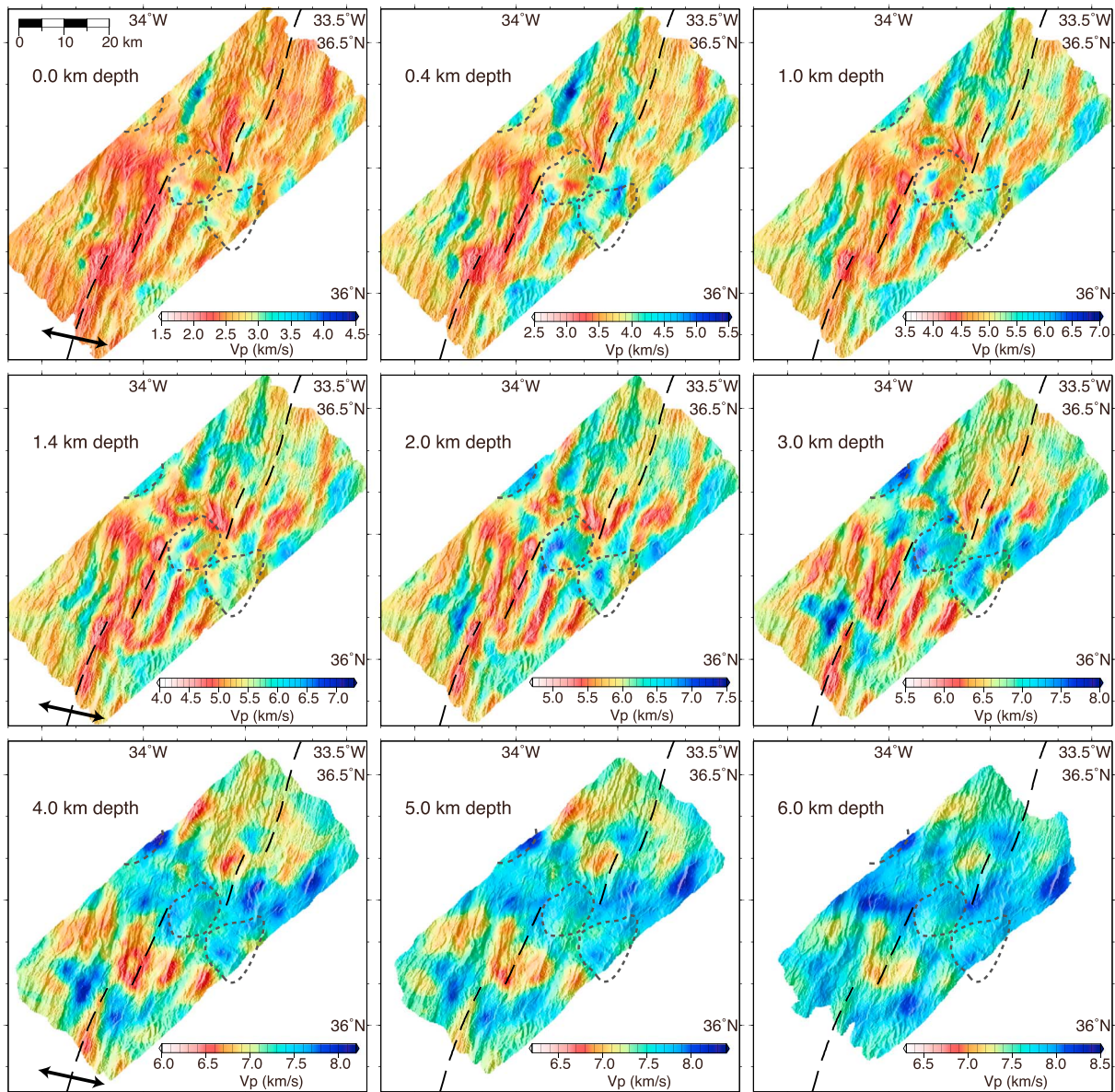
Figure 6. Map view slices of *P* wave velocity structure at different depths. (Slices parallel the seafloor.) Images are shaded by seafloor bathymetric slope to highlight relationships between seismic and tectonic features. Each panel has a unique color scale to highlight the velocity variations. Gray dashed curves outline the locations of the Rainbow, Pot of Gold, and Clurichaun massifs, as in Figure 1. Ridge segments and spreading direction are indicated by black dashed lines and arrows, respectively.

bathymetric wake of the Rainbow NTD (Figure 6). At 3 km depth, this band is somewhat wider than the surface width of the Rainbow massif and broadens with increasing depth. The highest velocities expected for a gabbroic lower crust (based on a variety of laboratory and seismic studies; see Christensen, 1979 and the summary in Dunn, 2015) are about 7.2 km/s. A map of the depth of the 7.2 km/s velocity isosurface, as a proxy for crustal thickness, is shown in Figure 9, in which this band is strongly evident. Reduced crustal thickness along the wake of the NTD is consistent with the deep bathymetry and high gravity values observed there (Paulatto et al., 2015). Shallow high-velocity regions (e.g., thin crust) also appear at the southern and northern NTDs, both of which are smaller ridge offsets that formed more recently. These variations in apparent crustal thickness can also be seen in a vertical seismic profile taken along the ridge axis, Figure 10, which shows that variations in the depth of the 7.2 km/s contour correspond with ridge segmentation. The contour is deeper near ridge segment centers and shallower near ridge offsets.

Each of the oceanic core complexes in the study area lies within the broad high-velocity wake of the Rainbow NTD, though the Clurichaun massif is at the edge of the experiment and only partly captured by the imaging. The massifs are underlain by a thinner-than-average seismic layer 2 and a deeper domed region of high velocities (Figure 4). The Rainbow massif is clearly an atypical feature as compared to the neighboring spreading centers and ridge offsets (Figure 10). Vertical cross sections through Rainbow are shown in Figure 11 at a variety of azimuths. In sections oriented roughly parallel to the plate boundary, the high-velocity region beneath the massif is elongate, mostly dome shaped, and broader than the topographic expression of the massif itself (Figure 11, profiles A and E). In cross sections oriented parallel to plate spreading, the high-velocity region is narrower, with an asymmetric wedge-shaped structure (Figure 11, profiles B and C) that extends upward to the seafloor. Flanking this high-velocity region (at most, but not all, azimuths) are areas of significantly lower-than-average V_P, especially in the depth range of 1–2 km below the seafloor. On the western and eastern sides of the massif, the velocity gradients between the high-velocity interior of the massif and the low-velocity flanking regions are sharp enough to produce seismic reflections, as observed in reflection images (Canales et al., 2017). The Rainbow hydrothermal vent area lies just west of the peak of the high-velocity wedge and above the high-velocity gradient on the west side of the wedge (Figure 7a).

6. Discussion

Seismic wave speed in the lithosphere is sensitive to composition, porosity (including crack density), temperature, and melt fraction. In this complex setting, separating the effects of these factors requires additional contextual information. We therefore draw on a variety of data sets from this area in the interpretation of the seismic images, including bathymetry and gravity (Paulatto et al., 2015), sonar backscatter (Eason et al., 2016), microseismicity (Horning, 2017), seismic reflection images (Canales et al., 2017), and seafloor sample compositions (Sigurdsson, 1981; Stakes et al., 1984; Fouquet et al., 1997; Gale et al., 2013; Andreani et al., 2014).

6.1. Crustal Structure

Away from the Rainbow NTD and its off-axis trace, several lines of evidence suggest that a crustal layer extends across the study area, for example, the pervasive volcanic nature of the seafloor (e.g., Eason et al., 2016; Parson et al., 2000; Stakes et al., 1984), the presence of high-backscatter axial neovolcanic zones and the mid-ocean ridge basalts sampled there (Sigurdsson, 1981; Stakes et al., 1984; Gale et al., 2013), and gravity and magnetic anomalies patterns (Paulatto et al., 2015). Using the depth of the 7.2 km/s isosurface as a rough proxy for crustal thickness (Figure 9), the average crustal thickness is estimated to be ~4.5–5 km away from the Rainbow NTD.

A low velocity layer within ~2 km of the seafloor (Figure 4a) is ubiquitous in oceanic crust. The values are too low for pore-free basaltic rocks, and the general interpretation is that the low velocities are due to fluid-filled cracks and pores, which greatly reduce wave speed (e.g., Swift et al., 1998). Anisotropy (Figure 4b) further indicates the presence of aligned cracks resulting from extensional stresses due to seafloor spreading. Confining pressures are too low to close such features at shallow depths (e.g., Swift et al., 1998), and studies of drill cores (e.g., Carlson, 2010), seafloor exposures (e.g., Christeson et al., 2010), and ophiolites (e.g., Gillis & Sapp, 1997) find significant porosity over this depth interval. Lateral variations in wave speed at these shallow depths can be attributed to variations in magmatic construction, including porosity and dike intrusion, fracturing, and hydrothermal sealing (e.g., Christeson et al., 2010). A cracked and porous upper crust is expected to be relatively cool, and P wave speeds are much less sensitive to low temperature variations (<500°C; e.g., Christensen, 1979) than porosity. In the upper crust, the lowest velocities tend to be located along the axes of the spreading centers (Figures 5 and 6), particularly along the segments located south of Rainbow. Relatively lower on-axis velocities and higher off-axis velocities in the upper crust are a global phenomenon and widely interpreted to reflect a decrease in porosity (and thus increase in velocity) with crustal age due to infilling of cracks and pores via hydrothermal deposition (e.g., Grevemeyer & Weigel, 1997; Houtz & Ewing, 1976; Purdy, 1987). In the study area, the aging trends appear to be overprinted by undulations in the velocity structure produced by faulting (discussed below).

The observed increase in velocity with increasing depth (Figure 4a) can be attributed to a reduction in pore volume with increasing pressure as pores close and decreasing vesicularity of lithologic units as rocks transition from primarily volcanic in nature to intrusive (e.g., Carlson, 2010; Swift et al., 1998). The average velocity profile is slower to ~4 km depth compared to crust formed at faster spreading ridges and other imaged areas
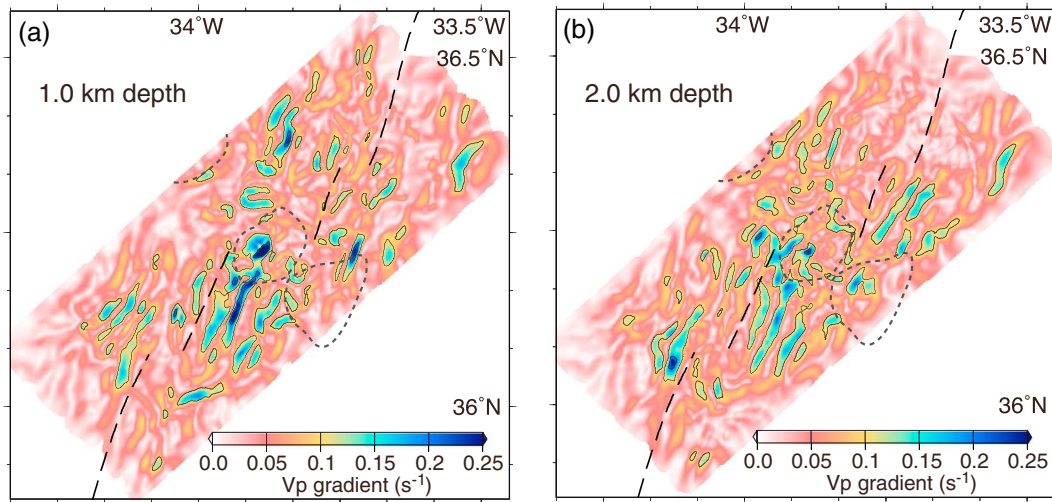
Figure 7. Map view slices of *P* wave velocity lateral gradient at depths of (a) 1.0 km and (b) 2.0 km. Linear high-gradient features mostly parallel major faults (or fault groupings). Ridge segments and massifs denoted as in Figure 6.

of the MAR (Figure 4a), suggesting a greater degree of porosity/cracks. This correlates with anisotropy extending to this depth (Figure 4b). The anisotropy indicates that the majority of stress-aligned cracks close by ~6 km depth. Since 4.5–5 km is about the average crustal thickness for the area (away from the Rainbow NTD), this suggests that the crustal section is on average cool enough to support pervasive tensile cracks. In a gabbro lithology, the temperature below which this is possible is uncertain but could be ~700–800°C (e.g., Manning et al., 2000).

At greater depths (>4 km), compositional variations, such as the transition from crust to mantle, play a more important role than porosity in controlling wave speed. Mantle velocities are often reported to be ~7.5 km/s and higher from field and laboratory studies (e.g., Dunn, 2015). Thus, the vertical change with increasing depth from 7.2 km/s (highest expected gabbroic velocities) to 7.5 km/s can be thought of as a crust-to-mantle transition zone. The images reveal a transition thickness of as much as 2 km in places. The broad nature of the transition could be due to magmatic processes, wherein melts freeze into the mantle lithosphere over a variety of depths, generating increasing proportions of crustal material with decreasing depth (Cannat, 1996; Kelemen et al., 2007). An alternate mechanism is serpentinization of the upper mantle via fluids that penetrate along faults, joints, and small cracks, lowering the mantle wave speed. While serpentinization may play an
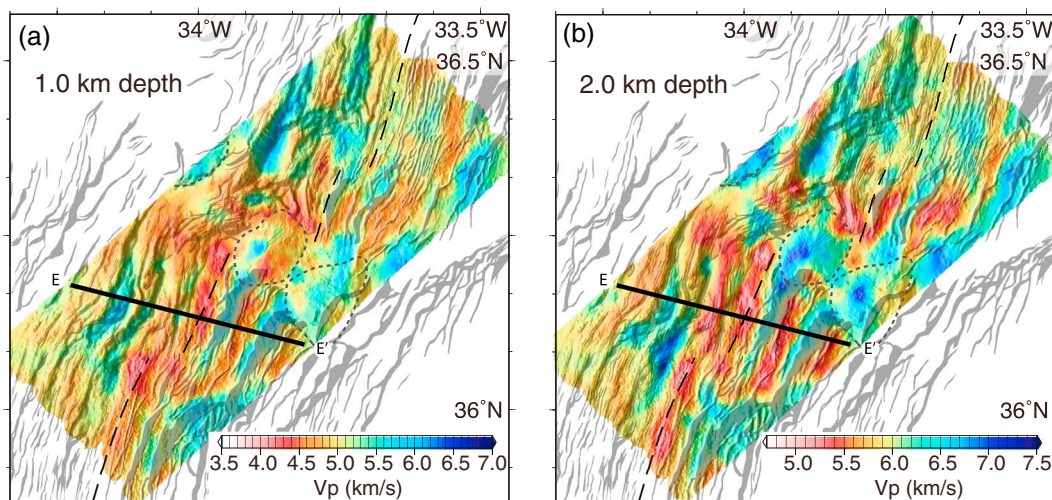

Figure 8. Map views of *P* wave velocity images (colors) with seafloor fault exposures (gray shading) from Paulatto et al. (2015) at (a) 1 and (b) 2 km depth, showing correlation of *P* wave velocity bands with seafloor fault surfaces. Solid line indicates location of profile E-E′ in Figure 5.
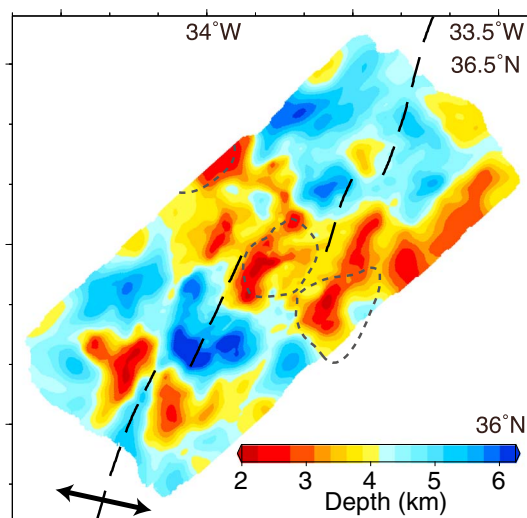
Figure 9. Map view of the depth of the 7.2 km/s velocity isosurface as a rough proxy for crustal thickness. Dashed lines indicate location of the ridge axes; arrows indicate spreading direction. Crustal thickness as estimated this way should be interpreted with caution, since other factors such as serpentinization (especially in the upper lithosphere across the Rainbow NTD) can be important.

important role, especially at the Rainbow NTD where mantle material reaches the seafloor, it is unlikely to be the dominant factor away from the Rainbow NTD. First, temperatures may be too hot to allow significant serpentinization (>350°C; Malvoisin et al., 2012). Second, if we were to assume that serpentinization played a primary role away from the Rainbow NTD at >3 km depth, then the counterintuitive result of this assumption would be that the higher-velocity, relatively amagmatic Rainbow NTD has undergone a lower degree of serpentinization than the lower-velocity, largely magmatic ridge axes. Instead, away from the NTD the proportions of crustal and mantle material probably dominate the deeper seismic variations (Figure 10d), with serpentinization acting as a secondary factor.

6.2. Magmatic Processes

Gravity maps (Paulatto et al., 2015) and seismic images (e.g., Figure 10) indicate along-axis variations in crustal thickness and by inference melt supply, with generally greater crustal thickness and melt supply near segment centers. However, there is little definitive evidence for large regions of sustained high temperatures in the lower crust and upper mantle at segment centers (or elsewhere). High temperatures reduce wave speeds with increasing effect approaching the solidus (e.g., Christensen, 1979; Kono et al., 2008); the presence of melt also strongly reduces wave speeds, even for low melt fractions (e.g., Schmeling, 1985). In Figure 5, there are deep low-velocity regions beneath the ridge axes, such as in profiles C and F (indicated with a black star), where velocity anomalies may reflect higher temperatures. However, these features are relatively subtle, with velocity values in the 6.8–7.2 km/s range, and their interpretation as large thermal anomalies or melt-containing regions is ambiguous. For comparison, the 35°N ridge segment of the MAR exhibits significantly lower velocities (6.4–6.6 km/s) in the lower crust (Figure 4a), with velocity perturbation contours opening downward, as would be expected for increasing temperature with depth (Dunn et al., 2005). In the study area, there is no evidence that melt is primarily supplied to the center of a ridge segment with subsequent shallow redistribution toward the segment ends (Smith & Cann, 1999). The simplest explanation, one that agrees with basic mantle upwelling and melt generation models (e.g., Kuo & Forsyth, 1988), is that the mantle melt supply varies along the ridge, with higher supply at segments centers, but without significant shallow redistribution.

In this study, and elsewhere along the axes of slow spreading ridges (e.g., Grimes et al., 2008), the evidence suggests that the lower crust is formed by repeated injection of small melt bodies rather than formed within a large transient crustal magmatic system as sometimes proposed (e.g., Dunn et al., 2005; Sinton & Detrick, 1992). A plumbing system characterized by small, widely spaced melt bodies is consistent with the lack of evidence for large subridge low-velocity regions. Similarly, magma storage in small, intermittent, and/or poorly connected reservoirs is consistent with observations that MAR basalts exhibit greater heterogeneity in mantle-derived (parental) magma compositions than those from higher supply areas such as the East Pacific Rise, where long-lived melt-rich storage areas tend to promote magma mixing and chemical homogenization (cf. Rubin & Sinton, 2007, and references therein). In addition, lavas sampled in the study area have relatively high MgO contents (>6.5 wt %, with an average of ~7.9 wt % MgO) (Gale et al., 2013; Sigurdsson, 1981; Stakes et al., 1984), suggesting that they did not spend significant time in the cool, shallow crust but instead erupted from deeper in the crust or upper mantle where ambient temperatures are higher (e.g., Sinton & Detrick, 1992). This is also consistent with evidence from other mid-ocean ridge basalt samples (e.g., Eason & Sinton, 2006; Grove et al., 1992; Herzberg, 2004), olivine melt inclusions (e.g., Wanless et al., 2015), and a variety of gabbros, megacrysts, and cumulate phases (e.g., Elthon, 1987; Stakes et al., 1984), indicating that magmas at slow spreading ridges partially crystallize in the lower crust and/or upper mantle prior to eruption. Both the seismic and petrologic observations suggest a model wherein low melt supply gives rise to a relatively thick lithosphere, and the repeated intrusion of small gabbroic bodies produces a gradual transition from mantle to increasing extents of crustal material upsection, until the lithosphere is dominated by crustal material at depths of ~ < 4–5 km.
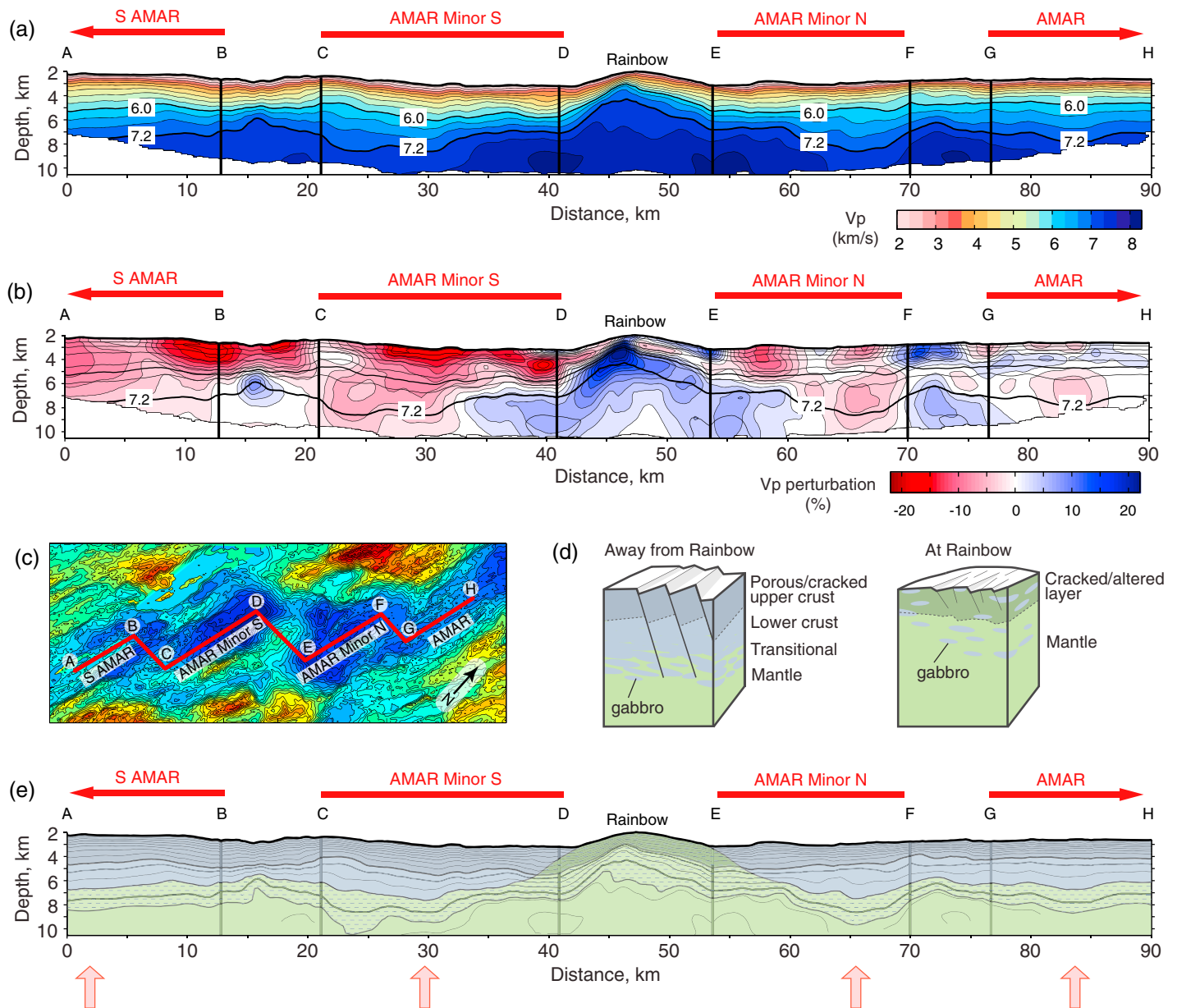
Figure 10. Vertical unfolded sections of image slices along the axes of the four ridge segments (as labeled). (a) Absolute velocity with a contour interval of 0.4 km/s. (b) Velocity perturbations relative to the 1-D average (Figure 4a) with a contour interval of 2%. Overlain on the velocity perturbation image are contours of V_P at 0.8 km/s spacing for reference. (c) Locations of each panel are indicated by red labeled lines on the map. (d) Basic interpretation of the seismic structure at and away from the Rainbow NTD. (e) Interpretation of the vertical velocity profile in terms of the explanation given in Figure 10d. Red arrows indicate regions along the axial segments where the crust appears to be thicker and melt supply is, by inference, relatively greater.

6.3. Faulting and Core Complex Formation

One of the more striking features observed in the seismic images is the undulations in *P* wave velocity structure (Figures 5–8) that correlate well with fault exposures, revealing the offset and rotation of the large crustal blocks that dominate abyssal hill formation. These offsets are most evident along AMAR Minor S, the segment just south of Rainbow, where the normal faults that bound the axial valley have some of the largest throws in the area (Paulatto et al., 2015). The bounding faults on the eastern side of the axial valley are particularly large (up to ~1.4 km) and are associated with some of the highest velocity gradients outside of the Rainbow massif (Figure 7). In vertical slices (Figure 5), areas with large vertical velocity offsets can be traced from the surface down to the 6.4 km/s contour, and some deeper, indicating that faults may extend across the entire crustal
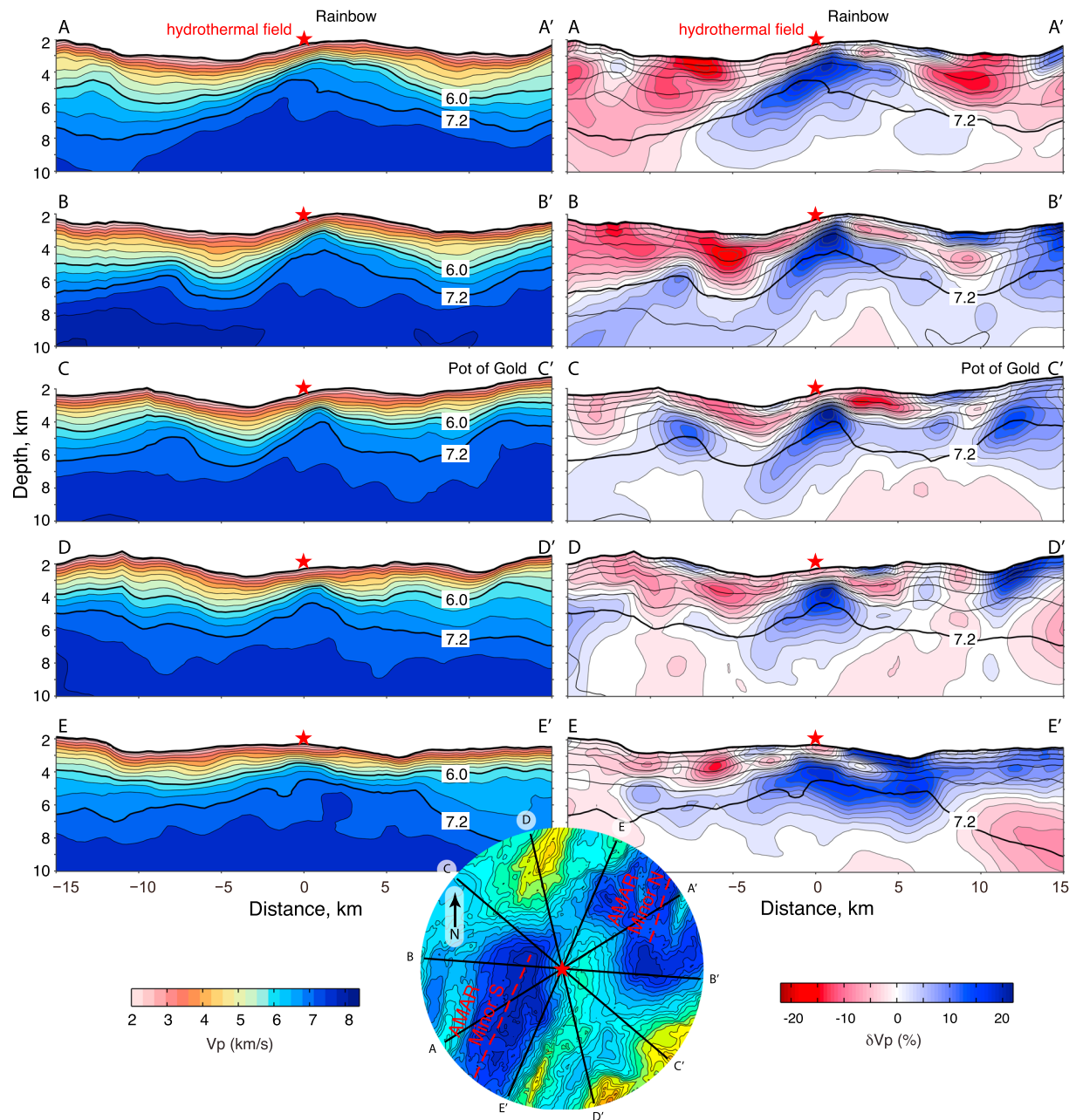
Figure 11. (left column) Vertical cross-section images of *P* wave velocity (contour interval is 0.4 km/s) and (right column) perturbation (2% contour interval), taken at different azimuths across the Rainbow massif (as indicated by the labeled black lines on the map inset). Overlain on the velocity perturbation images are contours of V_P at 0.8 km/s spacing for reference. All profiles are centered on the vent field (red star).

section within a few kilometers of the ridge axis. The trace of these offsets is hard to follow but appears to have a slight concave form in the images, with dip angles increasing from the seafloor downward. This structure is consistent with models of fault development at slow spreading ridges as estimated by bathymetric and microseismicity studies (deMartin et al., 2007; MacLeod et al., 2009). Extreme examples of extended crust appear on the western and eastern sides of the ridge in Figure 5, profiles A and G, respectively. However, the imaging is unable to resolve individual fault planes, and the observed features reflect the cumulative effect of groups of closely spaced faults.

Seismic and gravity data show that crustal thickness drops rapidly as the Rainbow NTD is approached from either the north or south. By inference, the overall melt supply also drops at the NTD and lithospheric

thickness is expected to increase. Along with these changes, the major faults that bound the axial valleys increase in throw and lateral separation approaching the NTD, culminating in core complex formation at the NTD itself. The now-inactive detachment fault at Rainbow is thought to be located on the western side of the massif, where bathymetry data show a clear break in slope between the massif and the neighbor valley floor (e.g., Andreani et al., 2014). Consistent with that location, seismic reflection images from the MARINER experiment show evidence for the detachment from an unconformity of flat reflectors against material with a different reflectivity structure (Figure 12a). From sonar bathymetry and backscatter images (Eason et al., 2016), the flat lying reflectors appear to be sedimented lava flows that fill the basin on the hanging wall above the downward trace of the fault.

The relationship between large offset detachment faults and adjacent smaller normal faults is still debated (e.g., Howell et al., 2016; Reston & Ranero, 2011; Smith et al., 2006). The axial bounding faults adjacent to OCCs have been proposed to consist of smaller "rider blocks" that overlie a detachment fault extending away from the OCC (Reston & Ranero, 2011). Alternatively, recent numerical modeling suggests that the transition from ridge flanking faults to long-lived OCC-forming detachment faults is the result of an along-axis transition in overall faulting style as magma supply decreases toward the OCC region (Howell et al., 2016; Tian & Choi, 2017). The relationship between the Rainbow detachment fault and neighboring faults is uncertain. The seismic tomography experiment cannot resolve individual fault planes, and MARINER seismic reflection profiles with an orientation favorable for imaging ridgeward dipping faults are concentrated on the Rainbow massif and do not sample adjacent lithosphere (Figure 1c). While there appears to be some semicontinuous relationship between the core complex and neighboring fault blocks for both Rainbow and Pot of Gold (Figure 6), offsets in the velocity contours, and locally lower velocities, mark the boundary between the massifs and fault blocks, suggesting relative motion between the two.

6.4. Rainbow Core Complex

Based on the presence of high gravity values (Paulatto et al., 2015), surface samples (Andreani et al., 2014), and the seismic high-velocity "wedge" beneath the massif, the massif appears to be dominated by uplifted mantle material containing lesser amounts of gabbroic intrusions (Figure 12b). Subhorizontal reflectors identified in reflection images suggest sill intrusions into the massif (Figure 12a; Canales et al., 2017). Assuming a V_P of 5 km/s for a 100% serpentinized peridotite (e.g., Horen et al., 1996), then the low V_P velocities that mostly cap and surround the interior high-velocity wedge (<5 km/s) are too low to be consistent with a pure serpentinite body; however, a mix of serpentinite with lesser amounts of altered gabbro and cracks/pores would be consistent with those velocities. The high-velocity wedge itself has values greater than that of pure gabbro (e.g., Miller & Christensen, 1997), but less than that of hot uplifted mantle, and can be explained by a mix of unaltered or lightly altered mantle plus scattered gabbroic intrusions. The 9 month microearthquake study of this area (Horning, 2017) detected over 65,000 events, the majority of which are confined to the high-velocity interior of the massif. These interior events do not line up along specific fault-like structures but instead establish a diffuse zone of deformation in a region where seismic velocities indicate largely ultramafic host rock above seismic reflectors interpreted to be magmatic sills driving hydrothermal convection in the ultramafic massif. The seismicity is consistent with brittle failure due to cooling stresses or stresses due to localized serpentinization.

The combination of microseismicity, velocity structure, serpentinization processes, and vent fluid compositions allows us to place some rough constraints on the thermal structure of the massif. The fluid chemistry, high temperatures, and output rates observed at the hydrothermal field strongly suggest a magmatic heat source (e.g., Charlou et al., 2002; Douville et al., 2002; German et al., 2010). One or more of the sills imaged within the massif (Canales et al., 2017) are thus likely still partially molten, supplying heat that drives fluid circulation. While locally high temperatures are required to drive the hydrothermal system, with estimated average peak temperatures >400°C, the abundance of microearthquakes within the interior of the massif indicates that much of the high V_P region above the deep melt lenses is cool enough to undergo brittle failure. In an olivine-dominated lithology, this suggests temperatures below ~600–750°C on average (e.g., McKenzie et al., 2005). Additionally, serpentinization reactions are most efficient at temperatures below ~350°C (Malvoisin et al., 2012), suggesting average temperatures within the interior of the massif exceed this; otherwise, pervasive alteration would produce much lower seismic velocities. In contrast, the low-velocity areas that cap the high-velocity interior probably reflect significant alteration and thus suggest temperatures <350°C.
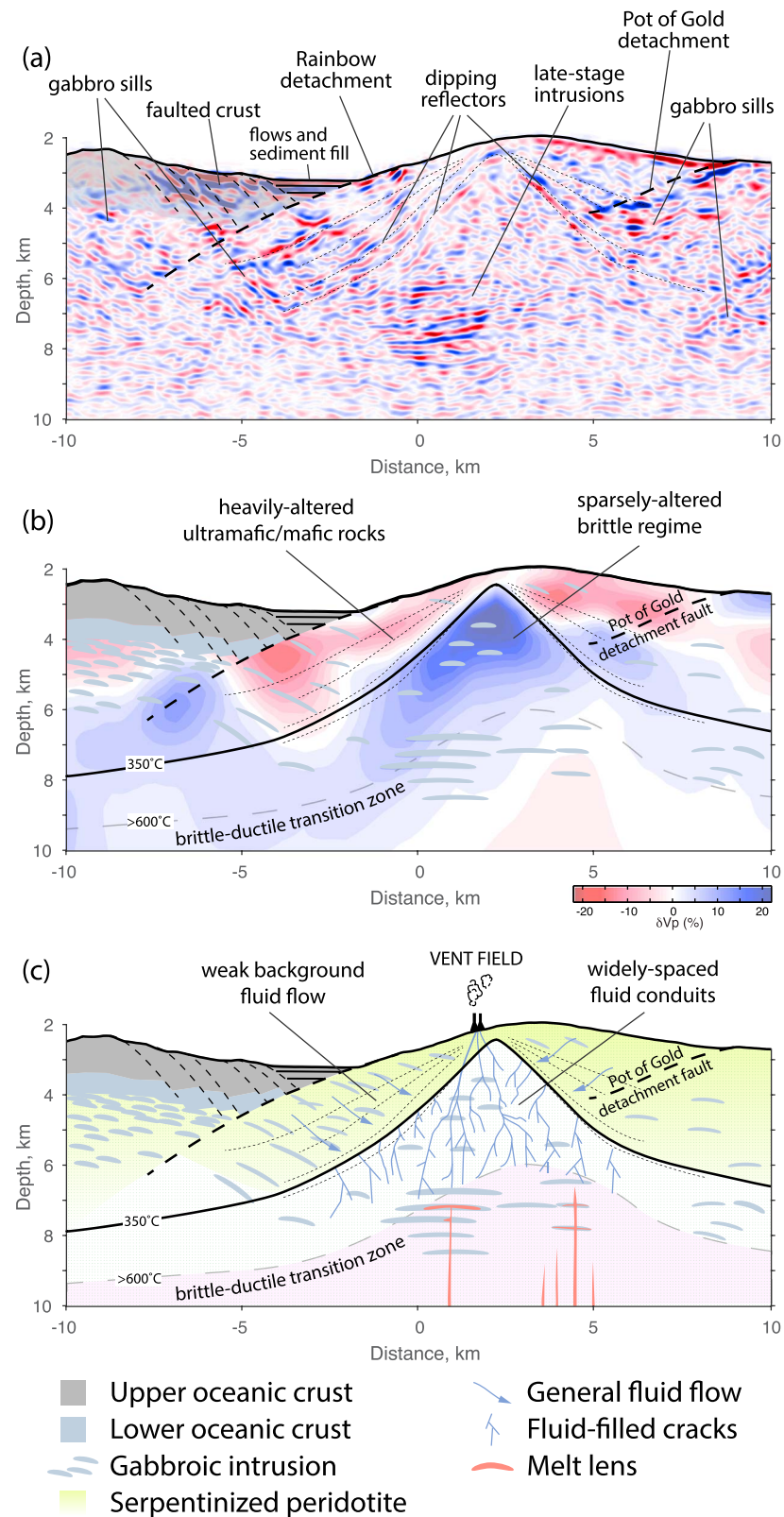
Figure 12. Interpretation of the seismic and other geological information (see text for discussion). (a) Seismic reflection image from Canales et al. (2017). Locations of Rainbow and Pot of Gold detachments are indicated on the plot, along with geologic interpretation. (b) Seismic tomographic image (slice oriented between B-B′ and C-C′ of Figure 11), along with geologic interpretation. (c) Cartoon interpretation of the Rainbow core complex internal structure.

We suggest that the thermal structure developed from the competing effects of heating from below (via repeated magma intrusions) and cooling from above (via cracking and fluid circulation) produces the relatively sharp seismic contact between the high-velocity but warm interior of the massif, where serpentinization is relatively inefficient, and the low-velocity cap that drapes the massif, where serpentinization reactions are very efficient. To date, the role of serpentinization on host permeability is not well quantified, with serpentinization thought to initially increase both porosity and diffusion of water on a fine scale (e.g., Tutolo et al., 2016) but to subsequently decrease bulk permeability by infilling of dominant fluid pathways (i.e., cracks and fractures) with reaction products (Farough et al., 2016). The hydrothermal vent fields on the Rainbow massif are closely associated with minor faults, suggesting most fluids within the upper parts of the massif circulate along these fault systems, and the surrounding heavily serpentinized rock may no longer be permeable in a relative sense.

Seismic reflection images show a series of dipping reflectors that follow the outline of the high-velocity wedge (Canales et al., 2017) (Figure 12a). It is unknown what these features represent. One interpretation is that they represent changes in the amount of alteration due to a series of temperature-controlled serpentinization and/or fluid mineralization reactions that occur over narrow temperature bands (e.g., Früh-Green et al., 2004). Alternatively, they may represent shear bands in weak serpentinite, due to massif uplift.

Figure 12c provides a cartoon of our suggested model for the interior structure of the Rainbow massif based on the observations discussed above. In summary, the Rainbow massif formed in a relatively low magma supply environment as a consequence of detachment faulting that led to mantle uplift. While principally of mantle composition, it is variably intruded with small gabbroic bodies and sparsely paved by surface basalt flows. The detachment fault is no longer active, and the massif has since been crosscut by minor faulting. Fluid circulation, driven by the heat of small cooling melt bodies intruded into the massif and channeled by thermal cracking and faulting, has altered the upper massif both physically and chemically. Thus, the top portions of the massif are heavily serpentinized, but this sharply contrasts with a warmer interior, where higher temperatures limit serpentinization. Within the interior, occasional magmatic intrusion keeps average temperatures over ~400°C. The boundary between the high-velocity interior and low-velocity exterior is relatively sharp, possibly modulated by the thermal structure generated by the episodic nature of melt intrusions. We suggest that new gabbroic sills are largely intruded deep in the massif within a brittle-ductile transition region. Between the shallow cold exterior and the deep brittle-ductile transition, fluids circulate along sparse crack networks and mine heat from intrusions and any remnant heat from the uplifted mantle itself. The presence of this crack network is demonstrated by tens of thousands of microearthquake events recorded in this region.

7. Conclusions

We present three-dimensional tomographic images of the crust and upper mantle in the Rainbow area using seismic P wave refraction data from the MARINER geophysical experiment. Based on these images and other available information, the major conclusions are as follows:

- A cold, brittle crustal layer of ~4–5 km thickness extends across the study area, except at the Rainbow NTD, where it is thin to nonexistent. Crustal thickness, and by inference melt supply, is greater near ridge segment centers than segment ends.
- The lower crust is formed by repeated injection of small melt bodies along the ridge axes rather than formed within large crustal magmatic systems or mush zones.
- There is no sharp crust-to-mantle lithological transition, a consequence of a thick thermal boundary layer leading to rising melts freezing into the crust and upper mantle at a variety of depths, generating increasing proportions of crustal material with decreasing depth.
- Fault offsets and throws increase toward the Rainbow NTD. Just to the north and south of the Rainbow offset, there are large rotated fault blocks observed in the tomographic images. This faulting appears to extend to at least the mantle, further evidence that the lower crust is generally cool and brittle near the ridge axis.
- The Rainbow massif consists of uplifted mantle material interspersed with gabbroic intrusions. The outer part of the massif is heavily altered, whereas the interior is relatively unaltered and deformable in the brittle regime.
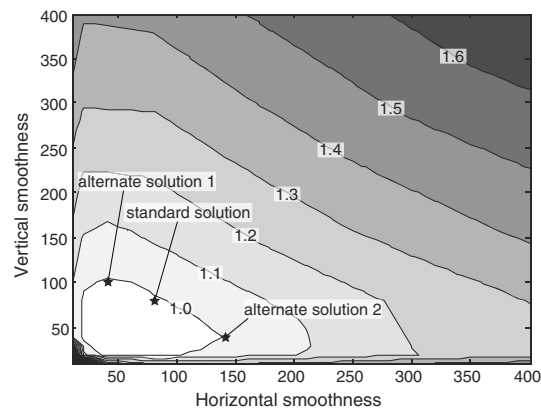
Figure A1. Normalized χ^2 misfit as a function of horizontal and vertical smoothness.

- Beneath the Rainbow hydrothermal vent field, fluid circulation is largely driven by the heat of small cooling melt bodies intruded into the base of the massif and channeled by deep thermal cracking and shallow fault networks.

Appendix A: Data Fit and Image Resolution

Spatial resolution and variance of the final tomographic image is controlled by image smoothness constraints. A grid search was performed by varying the strength of separate horizontal and vertical smoothness values to determine an acceptable range of solutions. With respect to the starting model, the traveltime data have a normalized chi-square misfit of 27. Acceptable models have a misfit of ~1, and the final model was chosen by this criterion and by examination of the results of checkerboard and spike resolution tests. Figure A1 shows the data misfit as a function of the smoothing parameters. Solutions with large smoothing values fit the data poorly. Very rough solutions also exhibit large data misfits, and their velocity structures are too rough to be constrained by the data on the basis of the Fresnel zone of the seismic waves and checkerboard tests. Models misfit of ~1 occur over a small range of smoothness values and are very similar in appearance. Figures in the text show the "standard" solution that was derived from equivalent values for horizontal/vertical smoothness (80/80). Alternative solutions, as indicated in Figure A1, are given in the supporting information accompanying this work and show a slight trade-off between models that have larger horizontal smoothing versus vertical smoothing. This trade-off arises from the principle that spatially narrow and tall features, or wide and short features, are better resolved than features that are both narrow and short. Tests using different damping values on the anisotropy portion of the solution also show that there are slight differences in the magnitude of velocity anomalies as this parameter is changed, but the pattern of the anomalies does not significantly change (see supporting information).

Figure A2 shows the results of checkerboard reconstructions using the same ray paths, matrix of partial derivatives (weighted by data uncertainties), and regularization constraints as for the standard solution. The result is shown for the first iteration of the forward and inverse problem; subsequent iterations improve the magnitudes of the checkers but not their form. The patterns are well resolved, especially within the station array bounds, but break down around the outer edge of the volume and below 7 km depth due to loss of ray coverage. Target checkerboard tests over the depth range of 8–10 km, where only ~2,000 rays sample in total, found that only large-scale features can be detected (>10 km), but not without significant smearing and distortion. Therefore, the images shown in the text are clipped at 8 km below the seafloor. Nevertheless, with an average crustal thickness of ~4 km, good lateral resolution is found over the upper 3–4 km of the mantle. Additional "spike tests" around the Rainbow massif area are shown in the lower half of Figure A2, where anomalies are assigned to an area spanned by eight neighboring model parameters (i.e., the smallest volume representable by the grid spacing). These tests are better at showing the amount of smearing within the central portions of the image and show good reconstruction of each spike, with a spike being properly located, but somewhat smeared out in the image. The smearing increases with increasing depth to 6.5 km, below which these anomalies are too small to be resolved. Additional checkerboard tests are provided in supporting information.
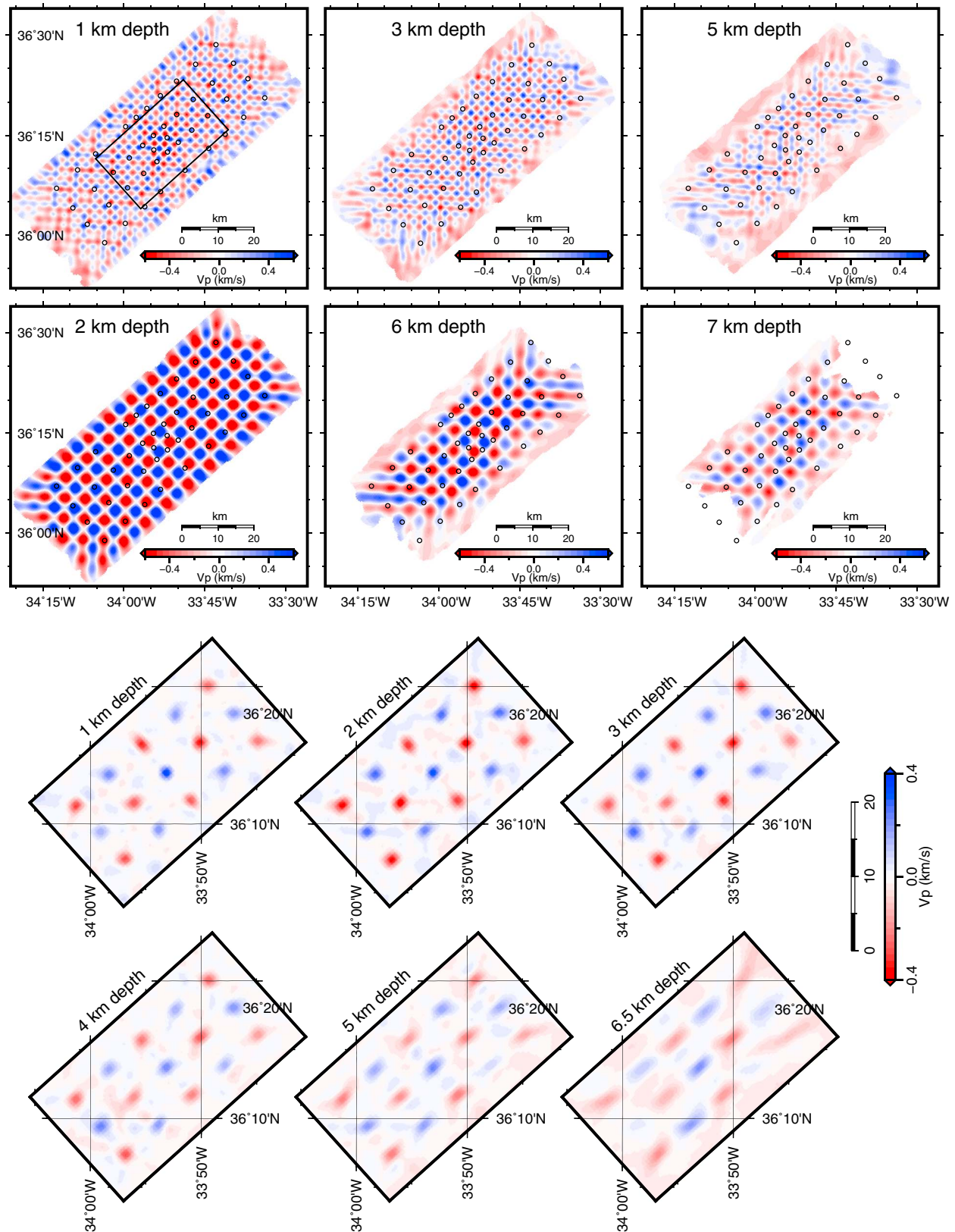
Figure A2. Checkerboard and spike test results. Map view slices (depth noted on each plot) where input anomalies were (first row) $2 \times 2 \times 2$ km^3 and (second row) $4 \times 4 \times 4$ km^3. The black box in the checkerboard plot at 1 km depth indicates the area spanned by spike test maps. (third and fourth rows) Map view slices from spike tests, each spike spans a set of eight neighboring model parameters (the parameter spacing is 500 m wide and vertically increases with depth from 250 m to 1 km).

References

Allen, D. E., & Seyfried, W. E. (2004). Serpentinization and heat generation: Constraints from Lost City and Rainbow hydrothermal systems. *Geochimica Et. Cosmochimica Acta*, 68, 1347–1354. https://doi.org/10.1016/j.gca.2003.09.003

Andreani, M., Escartín, J., Delacour, A., Ildefonse, B., Godard, M., Dyment, J., … Fouquet, Y. (2014). Tectonic structure, lithology, and hydrothermal signature of the Rainbow massif (Mid-Atlantic Ridge 36°14′N). *Geochemistry, Geophysics, Geosystems*, 15, 3543–3571. https://doi.org/10.1002/2014GC005269

Argus, D. F., Gordon, R. G., & DeMets, C. (2011). Geologically current motion of 56 plates relative to the no-net-rotation reference frame. *Geochemistry, Geophysics, Geosystems*, 12, Q11001. https://doi.org/10.1029/2011GC003751

Behn, M. D., & Ito, G. (2008). Magmatic and tectonic extension at mid-ocean ridges: 1. Controls on fault characteristics. *Geochemistry, Geophysics, Geosystems*, 9, Q08O10. https://doi.org/10.1029/2008GC001965

Bird, P. (2003). An updated digital model of plate boundaries. *Geochemistry, Geophysics, Geosystems*, 4(3), 1027. https://doi.org/10.1029/2001GC000252

Blackman, D. K., & Collins, J. A. (2010). Lower crustal variability and the crust/mantle transition at the Atlantis Massif oceanic core complex. *Geophysical Research Letters*, 37, L24303. https://doi.org/10.1029/2010GL045165

Buck, W. R., Lavier, L. L., & Poliakov, A. N. B. (2005). Modes of faulting at mid-ocean ridges. *Nature*, 434, 719–723. https://doi.org/10.1038/nature03358

Canales, J. P., Collins, J. A., Escartín, J., & Detrick, R. S. (2000). Seismic structure across the rift valley of the Mid-Atlantic Ridge at 23°20′ (MARK area): Implications for crustal accretion processes at slow spreading ridges. *Journal of Geophysical Research*, 105(B12), 28411–28425. https://doi.org/10.1029/2000JB900301

Canales, J. P., Detrick, R. S., Lin, J., Collins, J. A., & Toomey, D. R. (2000). Crustal and upper mantle seismic structure beneath the rift mountains and across a nontransform offset at the Mid-Atlantic Ridge (35°N). *Journal of Geophysical Research*, 105(B2), 2699–2719. https://doi.org/10.1029/1999JB900379

Canales, J. P., Dunn, R. A., Arai, R., & Sohn, R. A. (2017). Seismic imaging of magma sills beneath an ultramafic-hosted hydrothermal system. *Geology*, 45(5), 451–454. https://doi.org/10.1130/G38795.1

Canales, J. P., Sohn, R. A., & deMartin, B. J. (2007). Crustal structure of the Trans-Atlantic Geotraverse (TAG) segment (Mid-Atlantic Ridge, 26°10′N): Implications for the nature of hydrothermal circulation and detachment faulting at slow spreading ridges. *Geochemistry, Geophysics, Geosystems*, 8, Q08004. https://doi.org/10.1029/2007GC001629

Cann, J. R., Blackman, D. K., Smith, D. K., McAllister, E., Janssen, B., Mello, S., … Escartín, J. (1997). Corrugated slip surfaces formed at ridge-transform intersections on the Mid-Atlantic Ridge. *Nature*, 385(6614), 329–332. https://doi.org/10.1038/385329a0

Cannat, M. (1996). How thick is the magmatic crust at slow spreading oceanic ridges? *Journal of Geophysical Research*, 101(B2), 2847–2857. https://doi.org/10.1029/95JB03116

Cannat, M., Mendel, V., Ruellan, E., Okino, K., Escartín, J., Combier, V., & Baala, M. (2006). Modes of seafloor generation at a melt-poor ultraslow-spreading ridge. *Geology*, 34, 605–608. https://doi.org/10.1130/G22486.1

Carlson, R. L. (2010). How crack porosity & shape control seismic velocities in the upper oceanic crust: Modeling downhole logs from Holes 504B and 1256D. *Geochemistry, Geophysics, Geosystems*, 11, Q04007. https://doi.org/10.1029/2009GC002955

Cave, R. R., German, C. R., Thompson, J., & Nesbitt, R. W. (2002). Fluxes to sediments underlying the Rainbow hydrothermal plume at 36°14′N on the Mid-Atlantic Ridge. *Geochimica et Cosmochimica Act*, 66(11), 1905–1923. https://doi.org/10.1016/S0016-7037(02)00823-2

Charlou, J. L., Donval, J. P., Fouquet, Y., Jean-Baptiste, P., & Holm, N. (2002). Geochemistry of high H_2 and CH_4 vent fluids issuing from ultramafic rocks at the Rainbow hydrothermal field (36°14′N, MAR). *Chemical Geology*, 191(4), 345–359. https://doi.org/10.1016/S0009-2541(02)00134-1

Chen, Y. J. (2004). Modeling the thermal state of the oceanic crust. In C. German, et al. (Eds.), *Mid-ocean ridges: Hydrothermal interactions between the lithosphere and the oceans, American Geophysical Union Geophysical Monograph* (Vol. 148, pp. 95–110).

Christensen, N. I. (1979). Compressional wave velocities in rocks at high temperatures and pressures, critical thermal gradients, and crustal low-velocity zones. *Journal of Geophysical Research*, 84(B12), 6849–6857. https://doi.org/10.1029/JB084iB12p06849

Christeson, G. L., Karson, J. A., & McIntosh, K. D. (2010). Mapping of seismic layer 2A/2B boundary above the sheeted dike unit at intermediate spreading crust exposed near the Blanco Transform. *Geochemistry, Geophysics, Geosystems*, 11, Q03015. https://doi.org/10.1029/2009GC002864

Dannowski, A., Grevemeyer, I., Ranero, C. R., Ceuleneer, G., Maia, M., Phipps Morgan, J., & Gente, P. (2010). Seismic structure of an oceanic core complex at the Mid-Atlantic Ridge. 22°19′N. *Journal of Geophysical Research*, 115, B07106. https://doi.org/10.1029/2009JB006943

deMartin, B. J., Sohn, R. A., Canales, J. P., & Humphris, S. E. (2007). Kinematics and geometry of active detachment faulting beneath the Trans-Atlantic Geotraverse (TAG) hydrothermal field on the Mid-Atlantic Ridge. *Geology*, 35, 711–714. https://doi.org/10.1130/G23718A.1

Detrick, R. S., Buhl, P., Vera, E., Mutter, J., Orcutt, J., Madsen, J., & Brocher, T. (1987). Multi-channel seismic imaging of a crustal magma chamber along the East Pacific Rise. *Nature*, 326(6108), 35–41.

Douville, E., Charlou, J. J., Oelkers, E. H., Bienvenu, P., Colon, C. F. J., Donval, J. P., … Appriou, P. (2002). The Rainbow vent fluids (36°14′N, MAR): The influence of ultramafic rocks and phase separation on trace metal content in Mid-Atlantic Ridge hydrothermal fluids. *Chemical Geology*, 184(1-2), 37–48. https://doi.org/10.1016/S0009-2541(01)00351-5

Dunn, R. A. (2015). Crust and lithospheric structure – seismic structure of mid-ocean ridges. In B. Romanowicz & A. Dziewonski (Eds.), *Treatise on Geophysics* (Vol. 1, 2nd ed.). UK: Elsevier Science.

Dunn, R. A., & Hernandez, O. (2009). Tracking blue whales in the eastern tropical Pacific with an ocean-bottom seismometer and hydrophone array. *The Journal of the Acoustical Society of America*, 126, 1084–1094. https://doi.org/10.1121/1.3158929

Dunn, R. A., Lekić, V., Detrick, R. S., & Toomey, D. R. (2005). Three-dimensional seismic structure of the Mid-Atlantic Ridge (35°N): Evidence for focused melt supply and lower crustal dike injection. *Journal of Geophysical Research*, 110, B09101. https://doi.org/10.1029/2004JB003473

Dunn, R. A., & Martinez, F. (2011). Contrasting crustal production and rapid mantle transitions beneath back-arc ridges. *Nature*, 469, 198–202. https://doi.org/10.1038/nature09690

Eason, D. E., Dunn, R. A., Canales, J. P., & Sohn, R. (2016). Segment-scale variations in seafloor volcanic and tectonic processes from multibeam sonar imaging, Mid-Atlantic Ridge Rainbow region (35°45′-36°35′N). *Geochemistry, Geophysics, Geosystems*, 17, 3560–3579. https://doi.org/10.1002/2016GC006433

Eason, D. E., & Sinton, J. M. (2006). Origin of high-Al N-MORB by fractional crystallization in the upper mantle beneath the Galápagos Spreading Center. *Earth and Planetary Science Letters*, 252, 423–436. https://doi.org/10.1016/j.epsl.2006.09.048

Elthon, D. (1987). Petrology of gabbroic rocks from the mid-Cayman rise spreading center. *Journal of Geophysical Research*, *92*(B1), 658–682. https://doi.org/10.1029/JB092iB01p00658

Farough, A., Moore, D. E., Lockner, D. A., & Lowell, R. P. (2016). Evolution of fracture permeability of ultramafic rocks undergoing serpentinization at hydrothermal conditions: An experimental study. *Geochemistry, Geophysics, Geosystems*, *17*, 44–55. https://doi.org/10.1002/2015GC005973

Fouquet, Y., Charlou, J. L., Ondréas, H., Radford-Knoery, J., Donval, J. P., Douville, E., … Ribeiro, A. (1997). Discovery and first submersible investigations of the Rainbow hydrothermal field on the MAR (36°14′N). *EOS. Transactions of the American Geophysical Union*, *78*, 832.

Früh-Green, G. L., Connolly, J. A., Plas, A., Kelley, D. S., & Grobéty, B. (2004). Serpentinization of oceanic peridotites: Implications for geochemical cycles and biological activity. In *The subseafloor biosphere at mid-ocean ridges*, *American Geophysical Union. AGU Monograph* (Vol. 144, pp. 119–136). Washington, DC: https://doi.org/10.1029/144GM08

Gaill, F., Ballu, V., Cannat, M., Crawford, W., Dyment, J., Escartin, J., … Zbinden, M. (2007). Cruise MoMARDREAM-Naut and other MoMAR experiments at Rainbow and Lucky Strike in Summer 2007. *InterRidge News*, *16*, 15–16.

Gale, A., Dalton, C. A., Langmuir, C. H., Su, Y., & Schilling, J.-G. (2013). The mean composition of ocean ridge basalts. *Geochemistry, Geophysics, Geosystems*, *14*, 489–518. https://doi.org/10.1029/2012GC004334

German, C. R., Parson, L. M., & HEAT Scientific Team (1996). Hydrothermal exploration near the Azores Triple Junction: Tectonic control of venting at slow-spreading ridges? *Earth and Planetary Science Letters*, *138*(1-4), 93–104. https://doi.org/10.1016/0012-821X(95)00224-Z

German, C. R., Thurnherr, A. M., Knoery, J., Charlou, J. L., Jean-Baptiste, P., & Edmonds, H. N. (2010). Heat, volume and chemical fluxes from submarine venting: A synthesis of results from the Rainbow hydrothermal field, 36N MAR. *Deep Sea Research Part I: Oceanographic Research Papers*, *57*, 518–527. https://doi.org/10.1016/j.dsr.2009.12.011

Gillis, K. M., & Sapp, K. (1997). Distribution of porosity in a section of upper oceanic crust exposed in the Troodos Ophiolite. *Journal of Geophysical Research*, *102*(B5), 10133–10149. https://doi.org/10.1029/96JB03909

Grevemeyer, I., & Weigel, W. (1997). Increase of seismic velocities in upper oceanic crust: The "superfast" spreading East Pacific Rise at 14°14′S. *Geophysical Research Letters*, *24*(3), 217–220. https://doi.org/10.1029/96GL04005

Grimes, C. B., John, B. E., Cheadle, M. J., & Wooden, J. L. (2008). Protracted construction of gabbroic crust at a slow spreading ridge: Constraints from 206Pb/238U zircon ages from Atlantis Massif and IODP Hole U1309D (30°N, MAR). *Geochemistry, Geophysics, Geosystems*, *9*, Q08012. https://doi.org/10.1029/2008GC002063

Grove, T. L., Kinzler, R. J., & Bryan, W. B. (1992). Fractionation of mid-ocean ridge basalt (MORB). In J. Phipps Morgan, D. K. Blackman, & J. M. Sinton (Eds.), *Mantle Flow and Melt Generation at Mid-Ocean Ridges*, *American Geophysical Union. AGU Monograph* (Vol. 71, pp. 281–310). Washington, DC.

Herzberg, C. (2004). Partial crystallization of mid-ocean ridge basalts in the crust and mantle. *Journal of Petrology*, *45*, 2389–2405. https://doi.org/10.1093/petrology/egh040

Hooft, E. E., Detrick, R. S., Toomey, D. R., Collins, J. A., & Lin, J. (2000). Crustal thickness and structure along three contrasting spreading segments of the Mid-Atlantic Ridge, 33.5°–35°N. *Journal of Geophysical Research*, *105*(B4), 8205–8226. https://doi.org/10.1029/1999JB900442

Horen, H., Zamora, M., & Dubuisson, G. (1996). Seismic waves velocities and anisotropy in serpentinized peridotites from Xigaze ophiolite: Abundance of serpentine in slow spreading ridge. *Geophysical Research Letters*, *23*(1), 9–12. https://doi.org/10.1029/95GL03594

Horning, G. (2017). Geophysical and geochemical constraints on the evolution of oceanic lithosphere from formation to subduction, PhD thesis, Massachusetts Institute of Technology/Woods Hole Oceanographic Institution Joint Program in Oceanography. https://doi.org/10.1575/1912/8722

Houtz, R., & Ewing, J. I. (1976). Upper crustal structure as a function of plate age. *Journal of Geophysical Research*, *81*(14), 2490–2498. https://doi.org/10.1029/JB081i014p02490

Howell, S., Ito, G., Behn, M. D., Olive, J.-A., Kaus, B., Popov, A., Mittelstaedt, E., & Morrow, T. (2016). Exploring tectonomagmatic controls on mid-ocean ridge faulting and morphology with 3-D numerical models. Abstract T33A-3013, 2016 Fall Meeting, AGU, San Francisco, CA, 12–16 Dec.

Ildefonse, B., Fouquet, Y., Hoise, E., Dyment, J., Gente, P., Thibaud, R., Bissessur, D., & Yatheesh, V. (2008). Geological mapping of the Rainbow Massif, Mid-Atlantic Ridge, 36°14′N. *Eos Trans. AGU, Fall Meet. Suppl., Abstract*, T43B-2028.

Kelemen, P. B., Kikawa, E., Miller, D. J., & Party, S. S. (2007). Leg 209 summary: Processes in a 20-km-thick conductive boundary layer beneath the Mid-Atlantic Ridge, 14–16 N. In *Proceedings of the Ocean Drilling Program, Scientific Results* (Vol. 209, pp. 1–33). College Station, TX: Ocean Drilling Program.

Kono, Y., Miyake, A., Ishikawa, M., & Arima, M. (2008). Temperature derivatives of elastic wave velocities in plagioclase (An51±1) above and below the order-disorder transition temperature. *American Mineralogist*, *93*, 558–564. https://doi.org/10.2138/am.2008.2591

Kuo, B.-Y., & Forsyth, D. W. (1988). Gravity anomalies of the ridge-transform system in the South Atlantic between 31 and 34.5° S: Upwelling centers and variations in crustal thickness. *Marine Geophysical Researches*, *10*(3-4), 205–232. https://doi.org/10.1007/BF00310065

Kuznetsov, V., Cherkashev, G., Lein, A., Shilov, V., Maksimov, F., Arslanov, K., … Tarasenko, D. (2006). 230Th/U dating of massive sulfides from the Logatchev and Rainbow hydrothermal fields (Mid-Atlantic Ridge). *Geochronometria*, *25*, 51–55.

Lartaud, F., de Rafelis, M., Oliver, G., Krylova, E., Dyment, J., Ildefonse, B., … Gaill, F. (2010). Fossil clams from a serpentinite-hosted sedimented vent field near the active smoker complex rainbow, MAR, 36°13′N: Insight into the biogeography of vent fauna. *Geochemistry, Geophysics, Geosystems*, *11*, Q0AE01. https://doi.org/10.1029/2010GC003079

Lartaud, F., Little, C. T. S., De Rafelis, M., Bayon, G., Dyment, J., Ildefonse, B., … Le Bris, N. (2011). Fossil evidence for serpentization fluids fueling chemosynthetic assemblages. *Proceedings of the National Academy of Sciences of the United States of America*, *108*, 7698–7703. https://doi.org/10.1073/pnas.1009383108

Lowell, R. P., Farough, A., Hoover, J., & Cummings, K. (2013). Characteristics of magma-driven hydrothermal systems at oceanic spreading centers. *Geochemistry, Geophysics, Geosystems*, *14*(6), 1756–1770. https://doi.org/10.1002/ggge.20109

MacLeod, C. J., Searle, R. C., Murton, B. J., Casey, J. F., Mallows, C., Unsworth, S. C., & Harris, M. (2009). Life cycle of oceanic core complexes. *Earth and Planetary Science Letters*, *287*, 333–344. https://doi.org/10.1016/j.epsl.2009.08.016

Malvoisin, B., Brunet, F., Carlut, J., Rouméjon, S., & Cannat, M. (2012). Serpentinization of oceanic peridotites: 2. Kinetics and processes of San Carlos olivine hydrothermal alteration. *Journal of Geophysical Research*, *117*, B04102. https://doi.org/10.1029/2011JB008842

Manning, C.E., MacLeod, C.J. & Weston, P. E. (2000). Lower-crustal cracking front at fast-spreading ridges: Evidence from the East Pacific Rise and the Oman ophiolite. *Special Papers-Geological Society of America*, pp. 261–272.

McCaig, A. M., & Harris, M. (2012). Hydrothermal circulation and the dike-gabbro transition in the detachment mode of seafloor spreading. *Geology*, 40, 367–370. https://doi.org/10.1130/G32789.1

McClain, K. J., & Lewis, B. T. R. (1982). Geophysical evidence for the absence of a crustal magma chamber under the northern Juan de Fuca Ridge: A contrast with ROSE results. *Journal of Geophysical Research*, 87(B10), 8477–8489. https://doi.org/10.1029/JB087iB10p08477

McKenzie, D., Jackson, J., Priestley, K., & K. (2005). Thermal structure of oceanic and continental lithosphere. *Earth and Planetary Science Letters*, 233, 337–349. https://doi.org/10.1016/j.epsl.2005.02.005

Miller, D. J., & Christensen, N. I. (1997). Seismic velocities of lower crustal and upper mantle rocks from the slow spreading Mid-Atlantic Ridge, south of the Kane transform zone (MARK). In J. A. Karson (Eds.), *Proc. ODP, Sci. Results* (pp. 437–454). College Station, TX: Ocean Drilling Program.

Minshull, T. A., & White, R. S. (1996). Thin crust on the flanks of the slow-spreading Southwest Indian Ridge. *Geophysical Journal International*, 125(1), 139–148. https://doi.org/10.1111/j.1365-246X.1996.tb06541.x

Olive, J. A., Behn, M. D., & Tucholke, B. E. (2010). The structure of oceanic core complexes controlled by the depth distribution of magma emplacement. *Nature Geoscience*, 3, 491–495. https://doi.org/10.1038/ngeo888

Parson, L., Gràcia, E., Coller, D., German, C., & Needham, D. (2000). Second-order segmentation: The relationship between volcanism and tectonism at the MAR, 38°N–35°40′N. *Earth and Planetary Science Letters*, 178(3-4), 231–251. https://doi.org/10.1016/S0012-821X(00)00090-X

Paulatto, M., Canales, J. P., Dunn, R. A., & Sohn, R. A. (2015). Heterogeneous and asymmetric crustal accretion: New constraints from multibeam bathymetry and potential field data from the Rainbow area of the Mid-Atlantic Ridge (36°15′N). *Geochemistry, Geophysics, Geosystems*, 16, 2994–3014. https://doi.org/10.1002/2015GC005743

Phipps Morgan, J., & Chen, Y. J. (1993). Dependence of ridge-axis morphology on magma supply and spreading rate. *Nature*, 364(6439), 706–708. https://doi.org/10.1038/364706a0

Planert, L., Flueh, E. R., Tilmann, F., Grevemeyer, I., & Reston, T. J. (2010). Crustal structure of a rifted oceanic core complex and its conjugate side at the MAR at 5°S: Implications for melt extraction during detachment faulting and core complex formation. *Geophysical Journal International*, 181, 113–126. https://doi.org/10.1111/j.1365-246X.2010.04504.x

Purdy, G. M. (1987). New observations of the shallow seismic structure of young oceanic crust. *Journal of Geophysical Research*, 92(B9), 9351–9362. https://doi.org/10.1029/JB092iB09p09351

Reston, T. J., & Ranero, C. R. (2011). The 3-D geometry of detachment faulting at mid-ocean ridges. *Geochemistry, Geophysics, Geosystems*, 12, Q0AG05. https://doi.org/10.1029/2011GC003666

Rubin, K., & Sinton, J. (2007). Inferences on mid-ocean ridge thermal and magmatic structure from MORB compositions. *Earth and Planetary Science Letters*, 260, 257–276. https://doi.org/10.1016/j.epsl.2007.05.035

Sauter, D., Cannat, M., Rouméjon, S., Andreani, M., Birot, D., Bronner, A., & Searle, R. (2013). Continuous exhumation of mantle-derived rocks at the Southwest Indian Ridge for 11 million years. *Nature Geoscience*, 6(4), 314–320. https://doi.org/10.1038/ngeo1771

Schmeling, H. (1985). Numerical models on the influence of partial melt on elastic, anelastic and electric properties of rocks. Part I: Elasticity and anelasticity. *Physics of the Earth and Planetary Interiors*, 41(1), 34–57. https://doi.org/10.1016/0031-9201(85)90100-1

Searle, R. C., & Escartín, J. (2004). The rheology and morphology of oceanic lithosphere and mid-ocean ridges. In C. R. German, J. Lin, & L. M. Parson (Eds.), *Mid-ocean ridges: Hydrothermal interactions between the lithosphere and oceans* (Vol. 148, pp. 63–93). Washington, DC: American Geophysical Union. https://doi.org/10.1029/148GM03

Shaw, P. R. (1992). Ridge segmentation, faulting and crustal thickness in the Atlantic Ocean. *Nature*, 358(6386), 490–493. https://doi.org/10.1038/358490a0

Shaw, P. R., & Lin, J. (1993). Causes and consequences of variations in faulting style at the Mid-Atlantic Ridge. *Journal of Geophysical Research*, 98(B12), 21,839–21,851. https://doi.org/10.1029/93JB01565

Sigurdsson, H. (1981). First-order major element variation in basalt glasses from the Mid-Atlantic Ridge—29°N to 73°N. *Journal of Geophysical Research*, 86(B10), 9483–9502. https://doi.org/10.1029/JB086iB10p09483

Sinha, M. C., & Louden, K. E. (1983). The oceanographer fracture zone—I. Crustal structure from seismic refraction studies. *Geophysical Journal of the Royal Astronomical Society*, 75(3), 713–736. https://doi.org/10.1111/j.1365-246X.1983.tb05007.x

Sinton, J., & Detrick, R. (1992). Mid-ocean ridge magma chambers. *Journal of Geophysical Research*, 97(B1), 197–216. https://doi.org/10.1029/91JB02508

Smith, D. K., & Cann, J. R. (1999). Constructing the upper crust of the Mid-Atlantic Ridge: A reinterpretation based on the Puna Ridge, Kilauea Volcano. *Journal of Geophysical Research*, 104(B11), 25,379–25,399. https://doi.org/10.1029/1999JB900177

Smith, D. K., Cann, J. R., & Escartín, J. (2006). Widespread active detachment faulting and core complex formation near 138°N on the Mid-Atlantic Ridge. *Nature*, 442, 440–443. https://doi.org/10.1038/nature04950

Stakes, D. S., Shervais, J. W., & Hopson, C. A. (1984). The volcanic-tectonic cycle of the FAMOUS and AMAR Valleys, Mid-Atlantic Ridge (36°47′N): Evidence from basalt glass and phenocryst compositional variations for a steady state magma chamber beneath the valley midsections, AMAR 3. *Journal of Geophysical Research*, 89(B8), 6995–7028. https://doi.org/10.1029/JB089iB08p06995

Stephen, R. A. (1981). Seismic anisotropy observed in upper oceanic crust. *Geophysical Research Letters*, 8(8), 865–868. https://doi.org/10.1029/GL008i008p00865

Swift, S. A., Lizarralde, D., Hoskins, H., & Stephen, R. A. (1998). Velocity structure in the upper ocean crust at Hole 504B from vertical seismic profiles. *Journal of Geophysical Research*, 103(B7), 15,361–15,376. https://doi.org/10.1029/98JB00766

Tian, X., & Choi, E. (2017). Effects of axially variable diking rates on faulting at slow spreading mid-ocean ridges. *Earth and Planetary Science Letters*, 458, 14–21. https://doi.org/10.1016/j.epsl.2016.10.033

Tivey, M. A., & Dyment, J. (2010). The magnetic signature of hydrothermal systems in slow spreading environments. *Geophysical Monograph Series*, 188, 43–66. https://doi.org/10.1029/2008GM000773

Toomey, D. R., Solomon, S. C., Purdy, G. M., & Murray, M. H. (1985). Microearthquakes beneath the median valley of the Mid-Atlantic Ridge near 23 N: Hypocenters and focal mechanisms. *Journal of Geophysical Research*, 90(B7), 5443–5458. https://doi.org/10.1029/JB090iB07p05443

Tucholke, B. E., Behn, M. D., Buck, W. R., & Lin, J. (2008). Role of melt supply in oceanic detachment faulting and formation of megamullions. *Geology*, 36, 455–458. https://doi.org/10.1130/G24639A.1

Tucholke, B. E., & Lin, J. (1994). A geological model for the structure of ridge segments in slow spreading ocean crust. *Journal of Geophysical Research*, 99(B6), 11,937–11,958. https://doi.org/10.1029/94JB00338

Tucholke, B. E., Lin, J., & Kleinrock, M. C. (1998). Megamullions and mullion structure defining oceanic metamorphic core complexes on the Mid-Atlantic Ridge. *Journal of Geophysical Research*, 103(B5), 9857–9866. https://doi.org/10.1029/98JB00167

Tutolo, B. M., Mildner, D. F., Gagnon, C. V., Saar, M. O., & Seyfried, W. E. (2016). Nanoscale constraints on porosity generation and fluid flow during serpentinization. *Geology*, *44*(2), 103–106. https://doi.org/10.1130/G37349.1

Wanless, V. D., Shaw, A. M., Behn, M. D., Soule, S. A., Escartín, J., & Hamelin, C. (2015). Magmatic plumbing at Lucky Strike volcano based on olivine-hosted melt inclusion compositions. *Geochemistry, Geophysics, Geosystems*, *16*, 126–147. https://doi.org/10.1002/2014GC005517

Wessel, P., & Smith, W. H. F. (1998). New improved version of the Generic Mapping Tools released. *Eos, Transactions American Geophysical Union*, *79*(47), 579. https://doi.org/10.1029/98EO00426